

Study of the gluon propagator in the large- N_f limit at finite temperature and chemical potential for weak and strong couplings

Jean-Paul Blaizot* and Andreas Ipp†
ECT*, Villa Tambosi, Strada delle Tabarelle 286,
I-38050 Villazano Trento, ITALY

Anton Rebhan‡
Institut für Theoretische Physik, Technische Universität Wien
Wiedner Hauptstrasse 8-10/136, A-1040 Wien, AUSTRIA.
(Dated: 9th June 2021)

At finite temperature and chemical potential, the leading-order (hard-thermal-loop) contributions to the gauge-boson propagator lead to momentum-dependent thermal masses for propagating quasiparticles as well as dynamical screening and Landau damping effects. We compare the hard-thermal-loop propagator with the complete large- N_f gluon propagator, for which the usually subleading contributions, such as a finite width of quasiparticles, can be studied at nonperturbatively large effective coupling. We also study quantitatively the effect of Friedel oscillations in low-temperature electrostatic screening.

I. INTRODUCTION

At finite temperature and chemical potential, propagators of elementary fields are modified importantly at soft momentum scales. At leading order, scalar fields acquire simple thermal mass terms, but fermions and gauge fields develop additional quasiparticle branches with complicated momentum dependent thermal masses for propagating modes, Landau damping cuts, and, in the case of gauge fields, poles for imaginary wave vectors corresponding to dynamical screening [1, 2, 3, 4, 5, 6].

While the physical singularities of propagators in a gauge theory are gauge-fixing independent [7], naive perturbation theory leads to gauge-fixing dependent results beyond leading order and requires (at least) resummation of the full nonlinear and nonlocal hard-thermal-loop (HTL) effective action [8] (see e.g. Ref. [9] for a recent review). It has also been found that thermodynamic quantities like the entropy of QCD can be understood well down to temperatures $T \gtrsim 3T_c$ with couplings as large as $g \approx 2$ by using HTL quasiparticles in Φ -derivable two-loop approximations [10] (see also [11]). One would therefore want to understand the underlying quasi-particle picture also at larger couplings. The success of those resummation techniques has been established so far only by comparison to lattice data, therefore an independent test is desirable. One possibility to go beyond HTL is the large flavor number (N_f) limit [12, 13, 14] in which thermodynamic quantities like pressure or entropy can be calculated to all orders in the effective coupling, at next-to-leading order of the $1/N_f$ expansion (which is of order N_f^0). In the large- N_f limit, the thermodynamic potential exhibits a non-trivial (non-monotonic) behavior when going from weak to strong coupling. As will be shown in a forthcoming paper [15], the latter is due to a corresponding nontrivial behavior of the next-to-leading order asymptotic mass of the quarks. However, the contributions of the gauge bosons, which are needed only to leading order in the large- N_f expansion, are of similar magnitude, and it is worth to study this propagator and its properties in detail, in particular how it compares with the corresponding HTL propagator.

The large- N_f gluon propagator is essentially abelian and one-loop, and some comparisons with the HTL propagator have been worked out previously in Ref. [16], however without discussing renormalization scale dependences that affect any approximate result in a quantum field theory. We also give full details on the required analytical continuations, and we include finite quark chemical potential.¹ In particular we investigate quantitatively the effect of Friedel oscillations in the screening of static charges at low temperature and ultrarelativistic density.

*Electronic address: blaizot@ect.it

†Electronic address: ipp@ect.it

‡Electronic address: rebhana@hep.itp.tuwien.ac.at

¹ An extension of the large- N_f gluon self-energy to finite mass, albeit in the weak coupling regime, can be found in Ref. [17], where transport coefficients are calculated in the large- N_f limit.

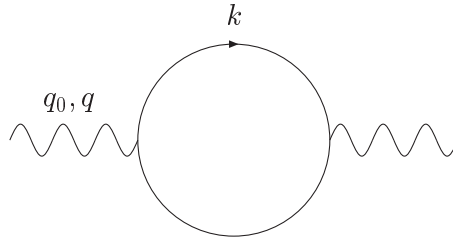


Figure 1: In the large- N_f limit, the leading contribution ($\sim N_f^0$) to the bosonic self-energy $\Pi_{\mu\nu}$ is given by this diagram with one fermion loop insertion.

II. LARGE- N_f QED AND QCD

In the large- N_f limit, an effective coupling $g_{\text{eff}}^2 = g^2 N_f/2$ (for QCD; $g_{\text{eff}}^2 = e^2 N_f$ for QED) is introduced which is kept of the order $g_{\text{eff}}^2 \sim O(1)$ as $N_f \rightarrow \infty$ and $g^2 \rightarrow 0$. All gluon-gluon interactions of QCD are suppressed by inverse powers of N_f – the theory becomes QED like. Also quark-gluon (or electron-photon) interactions are suppressed unless they form a new fermion loop. The leading contribution to the gauge boson self energy is therefore simply given a fermion loop (Fig. 1), which is trivially gauge independent. Dyson resummation of this contribution turns the gauge boson propagator into a nonperturbative object.

At large N_f , QCD loses asymptotic freedom. The scale dependence of the coupling in this limit is completely determined by the one-loop beta function

$$\beta(g_{\text{eff}}^2) \equiv \frac{\bar{\mu} \partial g_{\text{eff}}^2}{\partial \bar{\mu}} = -\frac{(g_{\text{eff}}^2)^2}{6\pi^2}. \quad (1)$$

Further corrections are suppressed by at least one power of $1/N_f$. Integrating this differential equation yields

$$\frac{1}{g_{\text{eff}}^2(\bar{\mu})} = \frac{1}{g_{\text{eff}}^2(\bar{\mu}')} + \frac{\ln(\bar{\mu}'/\bar{\mu})}{6\pi^2}, \quad (2)$$

which implies a Landau pole at $\Lambda_L \sim \bar{\mu} e^{6\pi^2/g_{\text{eff}}^2(\bar{\mu})}$.

The presence of a Landau pole means that large- N_f QED and QCD only exist as a cutoff theory. However, at finite temperature and chemical potential, where one is primarily interested in thermal effects, the presence of a cutoff can be neglected as long as $T, \mu \ll \Lambda_L$. This requires that g_{eff}^2 with renormalization scale of the order of temperature T or chemical potential μ , respectively, has to remain smaller than ~ 36 , giving enough room for testing the extension of hard-thermal-loop expansions from weak to stronger coupling.²

III. LARGE- N_f GAUGE BOSON PROPAGATOR

For definiteness, we shall use the Coulomb gauge and decompose the gauge propagator into a longitudinal and a transverse contribution

$$\begin{aligned} G_{00}(Q) &= G_L(Q), \\ G_{ij}(Q) &= \left\{ \delta_{ij} - \frac{q_i q_j}{q^2} \right\} G_T(Q), \end{aligned} \quad (3)$$

where the corresponding self-energy components are defined through

$$\begin{aligned} G_L(Q) &= \frac{-1}{q^2 + \Pi_L(Q)}, \\ G_T(Q) &= \frac{1}{-Q^2 + \Pi_T(Q)}, \end{aligned} \quad (4)$$

² The consequences of a Landau pole in thermal scalar field theory have been studied previously in Refs. [18, 19].

with Minkowski metric $(+, -, -, -)$ for the 4-dimensional momenta $Q = (q_0, \mathbf{q})$, i.e. $Q^2 = q_0^2 - q^2$. The corresponding spectral functions are determined through the discontinuity of the Feynman propagator along the Minkowski axis

$$\rho(q_0, q) \equiv \frac{1}{i} (G(q_0 + i\epsilon, q) - G(q_0 - i\epsilon, q)). \quad (5)$$

Propagating modes correspond to peaks in the spectral function. In the case of HTL, those peaks are given by infinitely narrow delta functions, but beyond the HTL approximation the peaks will acquire a finite width. Such peaks usually³ indicate the vicinity of a pole of the propagator to the real axis, but since the propagator does not exhibit a pole in the physical sheet, we have to extend our search to the unphysical sheet by analytic continuation. The position of this pole can be extracted numerically from the zero of the inverse propagator by specifying either q and extracting $q_0(q)$ from $G^{-1}(q_0(q), q) = 0$ or by specifying q_0 and solving $G^{-1}(q_0, q(q_0)) = 0$. In the former case, we obtain information about the frequency $\omega(q) = \text{Re } q_0(q)$ and the decay constant $\gamma(q) = \text{Im } q_0(q)$ for a propagating mode with given real-valued wave-vector q , which directly appears as a peak in the corresponding spectral function. In the latter case, we obtain the complex wave-vector $q(\omega)$ of a mode induced by a perturbation with a given real-valued frequency ω . In the static limit $\omega \rightarrow 0$ we can extract the Debye mass from the longitudinal component $G_L^{-1}(q_0 \rightarrow 0, im_D) = 0$. The transverse component is not screened in the static case, but exhibits dynamical screening for non-zero frequency.

A. Analytic continuation and scale dependence

The main technical difficulty in finding the poles of the propagator of Eq. (4), or correspondingly the zeros of the inverse propagator, is the correct analytic continuation of the self-energies from the physical sheet into the neighbouring unphysical sheet. The propagator $G(\omega + i\epsilon, q)$ neither contains poles for $\epsilon > 0$ nor for $\epsilon < 0$, but these two analytic regions are separated by a discontinuity along $\epsilon = 0$. In order to obtain the correct pole, one has to analytically continue the function $G(\omega + i\epsilon, q)$ across this separating line from $\epsilon > 0$ to $\epsilon < 0$.

The self-energy components that appear in the propagator (4) can be split into a thermal piece and a vacuum piece

$$\begin{aligned} \Pi_L(Q) &= \Pi_{L,\text{th}}(Q) - \frac{q^2}{Q^2} \Pi_{\text{vac}}(Q), \\ \Pi_T(Q) &= \Pi_{T,\text{th}}(Q) + \Pi_{\text{vac}}(Q), \end{aligned} \quad (6)$$

where the thermal pieces can be expressed as one-dimensional integrals (see Appendix A), while the vacuum part depends on a renormalization scale $\bar{\mu}$, and in the modified minimal subtraction ($\overline{\text{MS}}$) scheme is given by

$$\Pi_{\text{vac}}(Q) = \frac{g_{\text{eff}}^2}{12\pi^2} Q^2 \left\{ \log \left(\frac{-Q^2}{\bar{\mu}_{\overline{\text{MS}}}^2} \right) - \frac{5}{3} \right\}. \quad (7)$$

The analytic continuation of this vacuum piece is straightforward, as one just has to move the branch cut of the logarithm appropriately. One possibility is to split up the logarithm $\log(-Q^2) \rightarrow \log(q + q_0) + \log(q - q_0)$. As the logarithm has a branch cut along the negative real axis, we would cross it for $\text{Re } q \pm \omega < 0$ when continuing $q_0 = \omega + i\epsilon$ from $\epsilon > 0$ to $\epsilon < 0$. In the first logarithm we should therefore place the branch cut along the negative imaginary axis, and in the second logarithm along the positive imaginary axis. It is useful to define

$$\log^\uparrow(z) := \log(iz) - \frac{i\pi}{2}, \quad (8)$$

$$\log^\downarrow(z) := \log(-iz) + \frac{i\pi}{2}, \quad (9)$$

where $\log(z)$ is the standard logarithmic function with a branch cut along the negative real axis. Then $\log^\uparrow(z)$ has the branch cut along the positive imaginary axis, $\log^\downarrow(z)$ has the branch cut along the negative imaginary axis, while they both agree to $\log(z) = \log^\uparrow(z) = \log^\downarrow(z)$ for $\text{Re}(z) > 0$. The analytically continued vacuum contribution can then be written by replacing

$$\log \left(\frac{q^2 - q_0^2}{\bar{\mu}_{\overline{\text{MS}}}^2} \right) \rightarrow \log^\downarrow(q + q_0) + \log^\uparrow(q - q_0) - \log(\bar{\mu}_{\overline{\text{MS}}}^2) \quad (10)$$

³ See however Ref. [20] for an interesting counterexample.

in equation (7).

The analytic continuation of the thermal self-energy functions turns out to be more involved. The expressions for $\Pi_{T,\text{th}}$ and $\Pi_{L,\text{th}}$, which are given in Appendix A, involve a one-dimensional integral over a real variable k that has to be evaluated numerically. One might assume that it suffices to rewrite the logarithms appearing in the integrands, similar to the vacuum contribution Π_{vac} , and leave the integration over the real variable k untouched. It turns out that this prescription does not give the correct analytic continuation for the functions $\Pi_{T,\text{th}}(q_0, q)$ and $\Pi_{L,\text{th}}(q_0, q)$, as one can convince oneself by observing a discontinuity in the second derivative of the self-energies at $\epsilon = 0$. Indeed, we have to be careful that the integration path for k stays away from logarithmic singularities or branch cuts as we approach and penetrate the border of the physical sheet. In order to obtain the proper analytic continuation we have to deform the k -integration path such that crossings with singular points from the logarithms will be avoided. Another subtlety involved is that the logarithmic arguments first have to be rewritten in such a way that it is possible at all to deform the integration path satisfactorily. Details of this procedure are given in Appendix B.

For later use we note that the general form of the analytically continued inverse transverse propagator can be written as

$$G_T^{-1}(Q) = -Q^2 + g_{\text{eff}}^2 T^2 f\left(\frac{Q}{T}\right) + \Pi_{\text{vac}}(Q) \quad (11)$$

where the renormalization scale $\bar{\mu}_{\overline{\text{MS}}}$ appears explicitly in the temperature-independent vacuum piece Π_{vac} and implicitly in the coupling $g_{\text{eff}}^2 = g_{\text{eff}}^2(\bar{\mu}_{\overline{\text{MS}}})$, but the scalar function $f(Q/T) = \Pi_T(g_{\text{eff}}, T, Q)/(g_{\text{eff}}^2 T^2)$ is independent of the renormalization scale $\bar{\mu}_{\overline{\text{MS}}}$ as Π_T is proportional to g_{eff}^2 in the large- N_f limit.

In the hard thermal loop (HTL) or hard dense loop (HDL) limit [21, 22], Π_L and Π_T are given by elementary functions (listed in Appendix A2). The HTL limit is derived by assuming soft external lines $Q \sim gT$. In this kinematical regime, the leading contribution is not only gauge independent (also beyond the large- N_f limit), but also formally independent of the renormalization scale, as the vacuum contribution Π_{vac} is suppressed by g^2 compared to the leading HTL result. This leading piece is of the order of the Debye mass (HTL/HDL quantities will be marked by a hat)

$$\hat{m}_D^2 = g_{\text{eff}}^2 \left\{ \frac{T^2}{3} + \frac{\mu^2}{\pi^2} \right\}, \quad (12)$$

which is the only scale in the HTL/HDL propagator. The HTL plasma frequency, the frequency above which there exist propagating longitudinal and transverse modes, is given by $\hat{\omega}_{\text{pl}}^2 = \hat{m}_D^2/3$; the effective mass of transverse modes in the limit of large momenta (asymptotic thermal mass) by $\hat{m}_\infty^2 = \hat{m}_D^2/2$.

In the large- N_f limit, there is no such simple scaling, and the shape of the dispersion relation could in principle depend on the coupling, the temperature, and the renormalization scale. We have a restriction through the exact renormalization dependence given by Eq. (1) which means that we can basically choose a scale for plotting the dispersion relations as the result does not change if we vary renormalization scale and coupling according to the β -function.

To see how this works, let us assume that we know the position of a pole of $G(Q)$, i.e. $G^{-1}(Q) = 0$. We want to show that $\bar{\mu} \partial G^{-1}(Q)/\partial \bar{\mu} = 0$ is also true, provided that g_{eff} and $\bar{\mu}$ follow the β -function $\beta(g_{\text{eff}}^2) \equiv \bar{\mu} \partial g_{\text{eff}}^2 / \partial \bar{\mu}$. We find that the derivative of (11)

$$\begin{aligned} \bar{\mu} \frac{\partial G_T^{-1}(Q)}{\partial \bar{\mu}} &= 0 + \beta(g_{\text{eff}}^2) \left(T^2 f\left(\frac{Q}{T}\right) + \frac{Q^2}{12\pi^2} \left(\ln \frac{-Q^2}{\bar{\mu}_{\overline{\text{MS}}}^2} - \frac{5}{3} \right) \right) + \frac{g_{\text{eff}}^2 Q^2}{12\pi^2} (-2) \\ &= \beta(g_{\text{eff}}^2) \left(+ \frac{Q^2}{g_{\text{eff}}^2} \right) - \frac{g_{\text{eff}}^2 Q^2}{6\pi^2} = 0 \end{aligned} \quad (13)$$

vanishes indeed, where we used $G_T^{-1}(Q) = 0$ to get from the first to the second line, and the large- N_f β -function Eq. (1) in the last line. Stated the other way round, we could have derived the β -function by demanding that $\partial G^{-1}(Q)/\partial \bar{\mu} = 0$ vanishes. A similar proof holds of course for the longitudinal component as well. Also the solution $\omega(q)$ given implicitly by $G^{-1}(\omega(q), q) = 0$ is independent of $\bar{\mu}_{\overline{\text{MS}}}$. Since the Landau pole is also a solution to the zeros of the inverse propagator $G^{-1}(\Lambda_{\text{Landau}}) = 0$, the position of the Landau pole also obeys the renormalization group equation. The same is also true for the Debye mass, which is the solution at zero frequency ω and purely imaginary q for the longitudinal propagator $G_L^{-1}(\omega = 0, q = im_D) = 0$.

Therefore, if we plot the large- N_f dispersion relations for a specific choice of the renormalization scale, we actually plot the curve for all couplings and renormalization scales that are connected to each other by the renormalization group equation. The only problem that we might run into is the presence of the Landau pole.

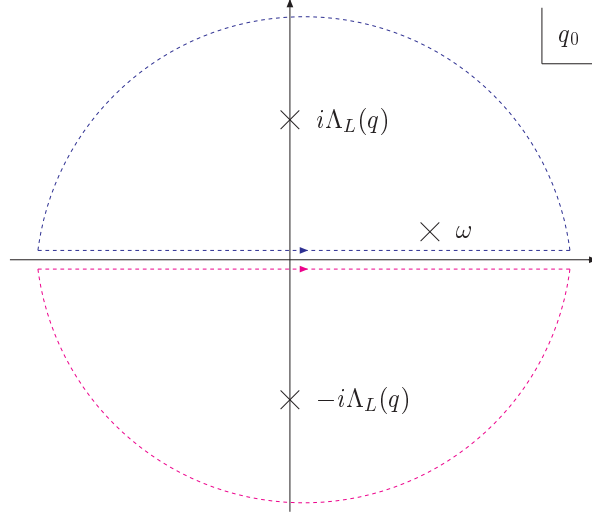


Figure 2: Integration path for the spectral function with three poles: One of those originates from the denominator $1/(q_0 - \omega)$, while the other two poles are the unavoidable Landau poles.

B. Sum rules including the Landau pole

Because of the presence of the Landau pole in the large- N_f theory, the basic spectral function sum rule

$$G(\omega, q) = \int_{-\infty}^{\infty} \frac{dq_0}{2\pi} \frac{\rho(q_0, q)}{q_0 - \omega}, \quad (14)$$

valid for complex ω , has to be modified. In the following, we will calculate the missing contribution. Let us first look at the zero temperature gauge field propagator. At zero temperature and zero chemical potential, $\Pi_T(q_0, q)$ and $\Pi_L(q_0, q)$ vanish, and one can analytically calculate the position of the Landau pole of the propagator (4) using only the vacuum self-energy (7). Solving for $G_T^{-1}(q_0, q) = 0$ we obtain

$$q^2 - q_0^2 = \bar{\mu}_{\text{MS}}^2 \exp\left(\frac{12\pi^2}{g_{\text{eff}}^2} + \frac{5}{3}\right) \equiv \Lambda_L^2. \quad (15)$$

We define the spectral function as the discontinuity of the boson propagator along the real q_0 axis

$$\begin{aligned} \rho_T(q_0, q) &\equiv \frac{1}{i} (G(q_0 + i\epsilon, q) - G(q_0 - i\epsilon, q)) \\ &= \frac{1}{i} (G(q_0 + i\epsilon, q) - G^*(q_0 + i\epsilon, q)) \\ &= 2\text{Im}G(q_0 + i\epsilon, q). \end{aligned} \quad (16)$$

The integral over the spectral function

$$\int_{-\infty}^{\infty} \frac{dq_0}{2\pi} \frac{\rho(q_0, q)}{q_0 - \omega} = \int_{-\infty}^{\infty} \frac{dq_0}{2\pi} \left(\frac{G(q_0 + i\epsilon, q)}{q_0 - \omega} - \frac{G(q_0 - i\epsilon, q)}{q_0 - \omega} \right) \quad (17)$$

can be calculated by closing the contour by a harmless grand half circle at infinity and picking up all pole contributions. The Landau pole (15) provides additional poles in the q_0 plane

$$q_0 = \pm i\sqrt{\Lambda_L^2 - q^2} \equiv \pm i\Lambda_L(q). \quad (18)$$

The first pole lies in the upper half of the complex plane and its residue can be calculated as:

$$\text{Res}_{q_0 \rightarrow i\Lambda_L(q)} \frac{G(q_0 + i\epsilon, q)}{q_0 - \omega} = \frac{6\pi^2}{g_{\text{eff}}^2} \frac{1}{i\Lambda_L(q) - \omega} \frac{1}{i\Lambda_L(q)}. \quad (19)$$

The pole in the lower half $q_0 = -i\Lambda_L(q)$ will receive an additional minus sign from the integration orientation, so that the total contribution (including the usual pole) is given by

$$\int_{-\infty}^{\infty} \frac{dq_0}{2\pi} \frac{\rho(q_0, q)}{q_0 - \omega} = G(\omega + i\epsilon, q) - \frac{12\pi^2}{g_{\text{eff}}^2} \frac{1}{\Lambda_L^2 - q^2 + \omega^2} \quad (20)$$

where we have substituted back $\Lambda_L^2(q) = \Lambda_L^2 - q^2$ with Λ_L as defined in (15).

With a full one-loop self energy insertion, the position of the Landau pole $\Lambda_L(q)$ as the solution to $G^{-1}(q_0 = \Lambda_L(q), q) = 0$ for a given q can in general only be calculated numerically. In the previous section we simply had $\Lambda_L(q) = \sqrt{\Lambda_L^2 - q^2}$, but the dependence on q is more complicated in the general case. Following the previous derivation for a general propagator, we can write the residue at the Landau pole as

$$\text{Res}_{q_0 \rightarrow i\Lambda_L(q)} \frac{G(q_0 + i\epsilon, q)}{q_0 - \omega} = \frac{1}{i\Lambda_L(q) - \omega} \left(\frac{\partial G^{-1}(q_0, q)}{\partial q_0} \Big|_{q_0 = i\Lambda_L(q)} \right)^{-1}. \quad (21)$$

Using the pole in the lower half plane and the property that the derivative of $G(q_0, q)$ is antisymmetric along the Euclidean axis $\partial G^{-1}(q_0, q)/\partial q_0|_{q_0 = -i\Lambda_L(q)} = -\partial G^{-1}(q_0, q)/\partial q_0|_{q_0 = i\Lambda_L(q)}$ ($G(q_0, q)$ is real and symmetric on the Euclidean axis, so its derivative is antisymmetric), the full relation is then given by

$$\int_{-\infty}^{\infty} \frac{dq_0}{2\pi} \frac{\rho(q_0, q)}{q_0 - \omega} = G(\omega + i\epsilon, q) - \frac{2\Lambda_L(q)}{\Lambda_L(q)^2 + \omega^2} \left(\frac{\partial G^{-1}(q_0, q)}{i\partial q_0} \Big|_{q_0 = i\Lambda_L(q)} \right)^{-1} \quad (22)$$

where the last part is real, despite the appearance of explicit “ i ”s. The last term corrects the usual spectral function sum rule due to the presence of the Landau pole. A rough estimate of the size of this correction can be obtained from the last term of (20): For small Q^2 it is around $5 \times 10^{-7} T^{-2}$ for $g_{\text{eff}}^2(\bar{\mu}_{\overline{\text{MS}}} = \pi T) = 9$ and around $2 \times 10^{-3} T^{-2}$ at $g_{\text{eff}}^2(\pi T) = 36$, and increases with increasing Q^2 . For soft momenta $Q \sim g_{\text{eff}} T$ one could estimate roughly that this term gives a correction to the propagator of the order of $(T/\Lambda_L)^2$. For hard momenta $Q \sim T$ the correction is of order $(T/g_{\text{eff}}\Lambda_L)^2$.

IV. RESULTS

A. Dispersion relations at zero chemical potential

Figure 3 recalls the pressure obtained in the large- N_f limit for finite temperature and zero quark chemical potential [12, 13, 14]. The full line gives the result at large N_f . The ambiguity introduced by varying the numerical cutoff below the Landau pole $Q_{\text{max}}^2 = a\Lambda_L^2$ between $a = 1/4$ and $1/2$ is shown as a tiny (red) band for large couplings. This ambiguity is suppressed by a factor $(T/\Lambda_L)^4$. Practically, this means that we can study a range of couplings $g_{\text{eff}}^2(\bar{\mu}_{\overline{\text{MS}}} = \pi T) \lesssim 36$ safely, where this number of course depends on the choice of renormalization scale $\bar{\mu}_{\overline{\text{MS}}}$ [a change of this scale changes the coupling according to Eq. (2)]. Perturbation theory ceases to work much sooner and shows large scale dependences for couplings already at $g_{\text{eff}}^2 \gtrsim 4$. Using an optimized renormalization scale, namely fastest apparent convergence of the effective mass parameter m_E (FAC-m), the perturbative result to order g_{eff}^5 follows the exact result up to $g_{\text{eff}}^2 \approx 8$. Still, there is a large range of couplings $8 \lesssim g_{\text{eff}}^2(\pi T) \lesssim 36$ to explore where strict perturbation theory fails, but the ambiguity introduced by the vicinity of the Landau pole is still negligible.

One of the remarkable and so far not easily understood features of the pressure curve is the minimum appearing at a coupling $g_{\text{eff}}^2(\pi T) \approx 14$. Paradoxically, in this strong coupling range $g_{\text{eff}}^2 \gtrsim 14$ the pressure seems to approach again the interaction-free pressure value. Since the nontrivial content of the large- N_f pressure can be expressed entirely in terms of the gauge boson propagator [12, 13, 14], it is natural to ask whether this nonmonotonic behavior is associated with qualitative changes in the properties of the gauge boson propagator. We shall find that this is not really the case. As will be shown in a subsequent paper [15], the nonmonotonic behavior is instead associated with nonmonotonic behavior of the asymptotic quark mass, which is a required ingredient when expressing the entropy in terms of quasiparticle spectral data [23, 24].

In the following we will plot spectral functions and dispersion relations covering weak and strong coupling for the gauge boson propagator in the large- N_f limit, and compare them to the corresponding HTL results. For larger couplings, the question of renormalization scale dependence becomes important. In principle one could plot the following comparisons between exact large- N_f and HTL results at various scales. To avoid cluttering the plots, we decided to scale large- N_f quantities by the large- N_f Debye mass m_D , and HTL quantities by the HTL Debye mass

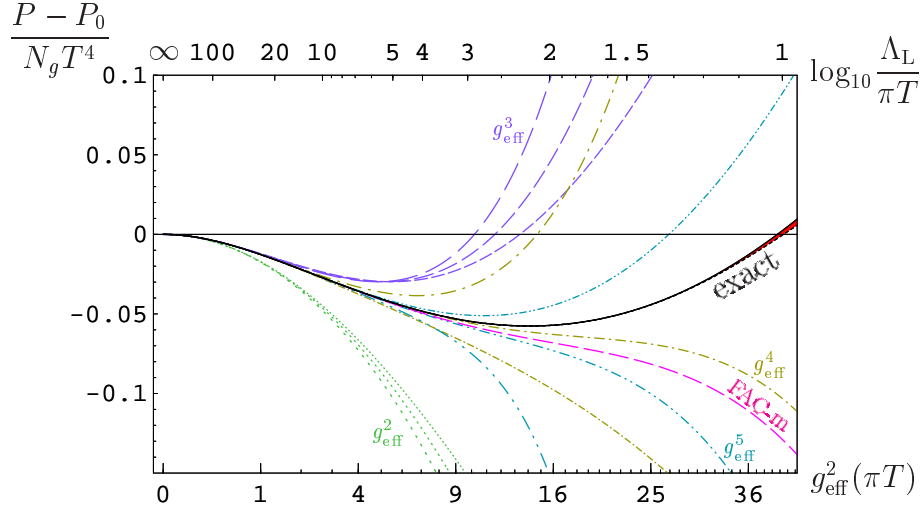


Figure 3: Exact result for the interaction pressure at finite temperature and zero chemical potential at large N_f as a function of $g_{\text{eff}}^2(\bar{\mu}_{\overline{\text{MS}}} = \pi T)$, compared to strict perturbation theory [12, 13, 14]. The tiny band appearing for large values of the coupling for the exact result shows the cutoff dependence from varying the upper numerical integration cutoff between $1/\sqrt{4} = 50\%$ and $1/\sqrt{2} \approx 70\%$ of the Landau pole Λ_L . The results of strict perturbation theory are given through order g_{eff}^2 (dotted line), g_{eff}^3 (dashed), g_{eff}^4 (dash-dotted), and g_{eff}^5 (dash-dot-dotted) where the renormalization scale $\bar{\mu}_{\overline{\text{MS}}}$ is varied between $\frac{1}{2}\pi T$ (line pattern slightly compressed), πT , and $2\pi T$ (line pattern slightly stretched). The line labelled “FAC-m” indicates the scale chosen by the prescription of fastest apparent convergence as indicated in the text for which the curves of g_{eff}^4 and g_{eff}^5 coincide.

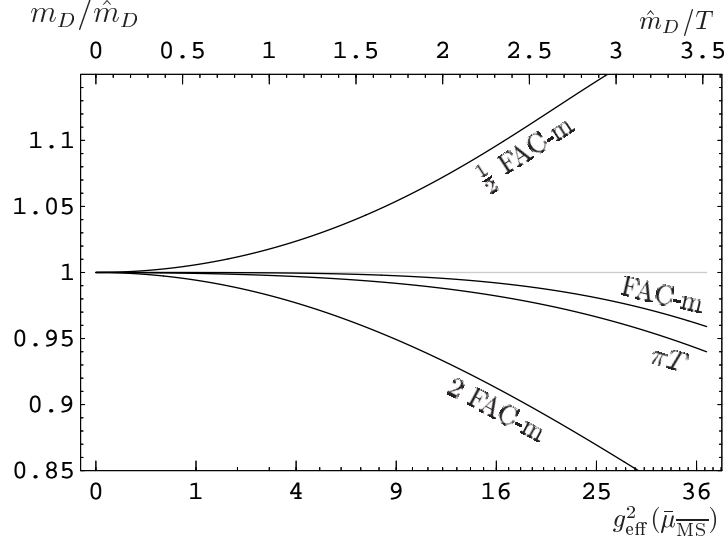


Figure 4: Comparison of the large- N_f Debye mass m_D to the corresponding HTL value \hat{m}_D . The renormalization scale $\bar{\mu}_{\overline{\text{MS}}}$ is varied by a factor of 4 around FAC-m. Using FAC-m or πT as the renormalization scale brings the HTL result within a few percent of the full result for the whole range of couplings g_{eff}^2 plotted. Note that the abscissa does not denote the coupling at a fixed scale, but at a different scales as indicated on the lines.

\hat{m}_D and present them in the same plot. Each of the quantities is then separately renormalization scale independent, while the renormalization scale dependence of the corresponding HTL approximations can be read off separately from a plot m_D/\hat{m}_D . (Note that the plasma frequency would be less appropriate to set a scale of the order $\sim gT$ because of the imaginary part it obtains at larger couplings g_{eff}^2 – the Debye mass on the contrary always stays purely real.) For the spectral functions we note that $g_{\text{eff}}^2 G(q_0, q)$ and therefore $g_{\text{eff}}^2 \rho(q_0, q)$ is a renormalization scale independent quantity.

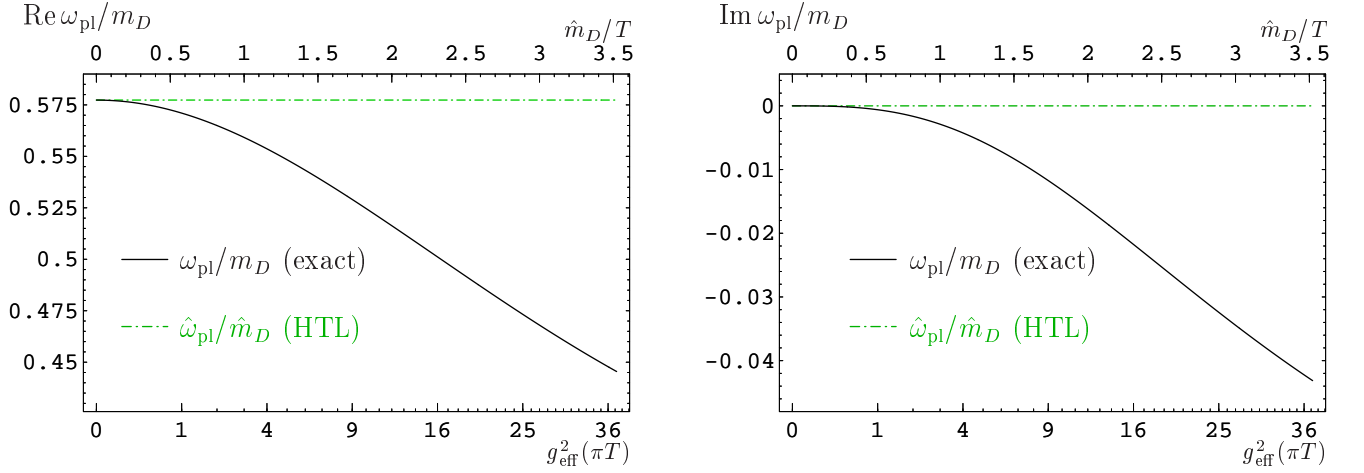


Figure 5: Real and imaginary part of the plasma frequency ω_{pl} in the large- N_f limit compared to the HTL value $\hat{\omega}_{\text{pl}}/\hat{m}_D = 1/\sqrt{3} \approx 0.577$ as a function of $g_{\text{eff}}^2(\bar{\mu}_{\overline{\text{MS}}} = \pi T)$ at the renormalization scale πT . The imaginary part of the plasma frequency, the damping constant, is caused by the vacuum process of quark-antiquark pair creation, and thus missing in the purely thermal HTL approximation.

One of the most prominent properties of the gauge boson propagator is the emergence of a screening mass in the static longitudinal sector, the Debye mass. Numerically, we obtain the Debye mass as the solution to Eq. (4) in the static limit,

$$q^2 + \Pi_L(q_0 = 0, q) = 0 \quad \text{at } q = im_D. \quad (23)$$

While in the HTL approximation $\hat{\Pi}_L(q_0 = 0, q) = \hat{m}_D^2$ is a constant given by Eq. (12), this is no longer the case for the complete expression in the large- N_f limit. Nevertheless, the solution for m_D indeed turns out to be a purely real number. The latter can be identified with the screening mass in a Yukawa potential for static sources. Figure 4 shows a comparison of the Debye mass in the large- N_f limit, normalized to its corresponding HTL value (12). Other than the following plots, the axis of Fig. 4 is not labelled at a fixed renormalization scale $g_{\text{eff}}^2(\pi T)$, but rather at a different scale for each curve as denoted next to each line. The four curves are in fact related by the renormalization group equation (2), because the position of the large- N_f Debye mass is renormalization scale independent, like any singularity of the propagator. The HTL result on the other hand is a truncated result at order g_{eff}^2 . Therefore the HTL Debye mass does not run properly with the renormalization scale, leading to a renormalization-scale dependence of m_D/\hat{m}_D .

For small g_{eff}^2 an optimal choice of renormalization scale is obtained by requiring that the g_{eff}^4 contribution to the Debye mass m_D for the full large- N_f result vanishes. This prescription of fastest apparent convergence will be labelled as FAC-m and leads to [12, 13, 14]

$$\bar{\mu}_{\overline{\text{MS}}}^{\text{FAC-m}} = e^{\frac{1}{2} - \gamma_E} \pi T \approx 0.9257 \pi T, \quad (24)$$

which is very close to the choice $\bar{\mu}_{\overline{\text{MS}}} = \pi T$, the lowest Matsubara frequency. Even for the largest couplings $g_{\text{eff}}^2 \approx 36$ the deviation from the HTL Debye mass is only of the order of 5% for this choice. It will therefore suffice to compare all following quantities at a fixed scale $\bar{\mu}_{\overline{\text{MS}}} = \pi T$, keeping in mind that a change of the scale e.g. by a factor of 2 will introduce additional deviations as displayed in Fig. 4.

Another quantity of central importance is the plasma frequency: It indicates the lowest frequency for which there exist propagating modes in the plasma. Transverse and longitudinal modes share the same plasma frequency in an isotropic plasma. Frequencies below the plasma frequency are associated with spatial screening. The plasma frequency and the frequency of propagating modes are obtained from

$$G_{L,T}^{-1}(\omega(q), q) = 0, \quad q \in \mathbb{R}. \quad (25)$$

While the dispersion relations obtained in the HTL approximation involve only real frequencies $\omega(q)$, the full large- N_f result is complex. Real and imaginary parts are plotted separately in Fig. 5. Compared to the real part, the magnitude of the imaginary part remains small for all values of the coupling. For small couplings, the plasma frequency approaches

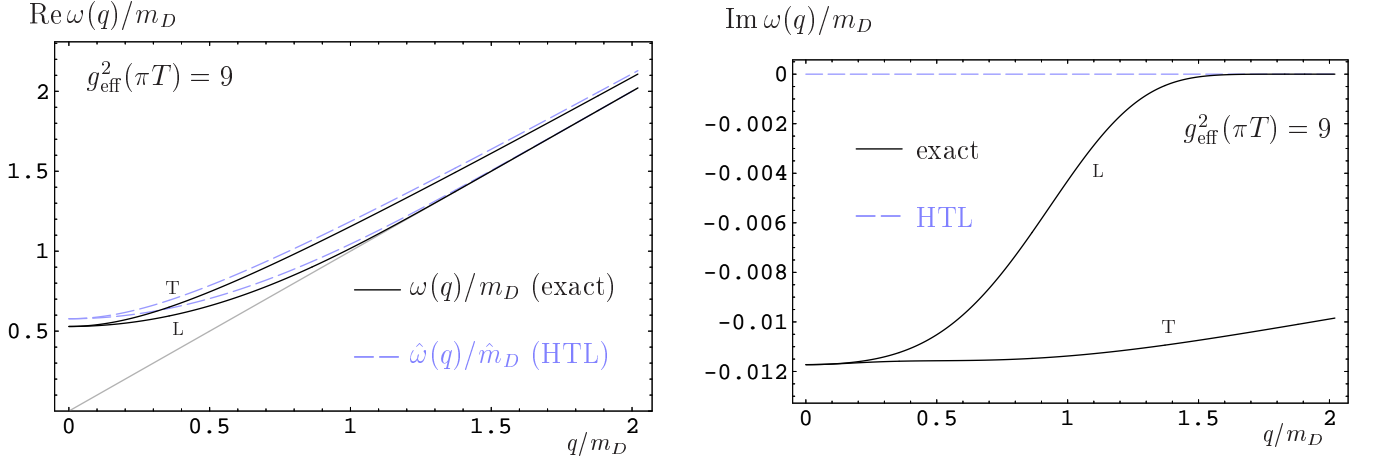


Figure 6: Real and imaginary part of the dispersion relation $\omega(q)$ as a function of real q for $g_{\text{eff}}^2 = 9$ in the large- N_f limit compared to the HTL result. Abscissa and ordinate for the exact large N_f result are scaled by the large- N_f Debye mass m_D , while the HTL curve is on both axis scaled by the HTL mass \hat{m}_D . At this moderate value of the coupling, which lies at the border of applicability of strict perturbation theory, the plasma frequency is slightly lowered and obtains a small imaginary part. The light gray line indicates the lightcone.

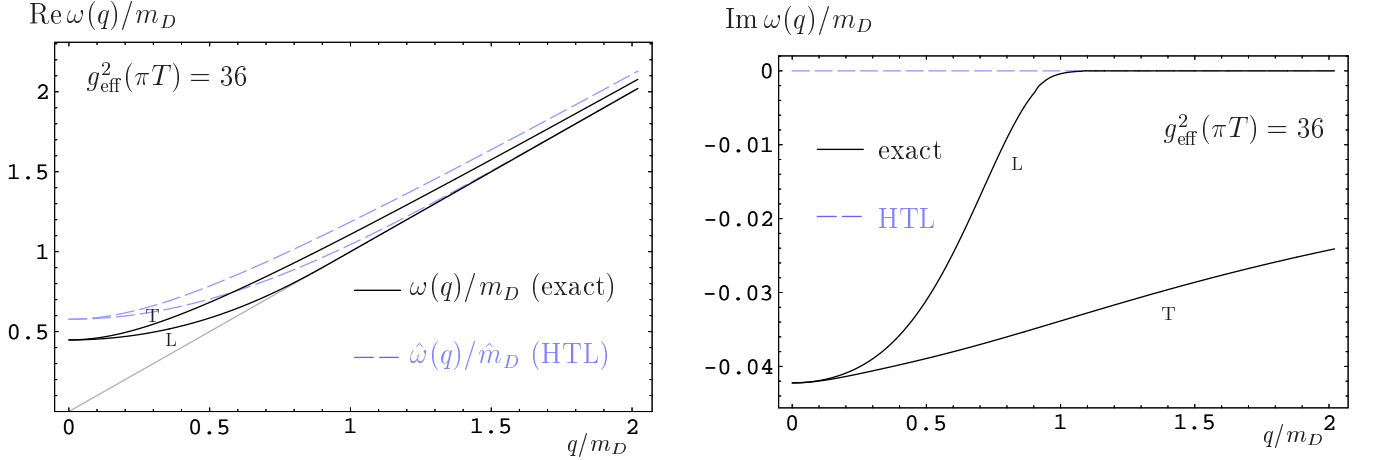


Figure 7: Same as Figure 6 for the larger coupling $g_{\text{eff}}^2(\pi T) = 36$. Real and imaginary part are further lowered compared to the case of $g_{\text{eff}}^2(\pi T) = 9$. As the longitudinal branch approaches the lightcone faster, also its imaginary part approaches 0 at smaller values of q/m_D .

the HTL value, which is given by $\hat{\omega}_{\text{pl.}} = \hat{m}_D/\sqrt{3} \approx 0.57735 \hat{m}_D$. As the coupling increases, the renormalization-scale independent ratio of plasma frequency to Debye mass decreases by 10% at $g_{\text{eff}}^2(\bar{\mu}_{\overline{\text{MS}}} = \pi T) = 14$ and by 20% at $g_{\text{eff}}^2 = 36$. The imaginary part is due to the vacuum process of quark-antiquark pair creation, which is missing in the HTL approximation. (In QCD at finite N_f , the damping rate of propagating bosonic modes is dominated by Bose-enhanced gluonic contributions proportional to a single power of g rather than to $g_{\text{eff}}^2 = g^2 N_F/2$ [25, 26, 27].)

Figures 6 and 7 show the dispersion curve for representative values of the coupling $g_{\text{eff}}^2(\bar{\mu} = \pi T) = 9$ and 36. These plots are scaled by the large- N_f plasma frequency and thus show a renormalization scale independent result. HTL quantities are scaled by the HTL Debye mass. One notes the lower plasma frequency compared to the corresponding HTL value, albeit the effect is moderate even at large coupling. The imaginary part of the longitudinal branch vanishes quickly as the curve approaches the light-cone. In the limit of vanishing q/m_D , the real as well as the imaginary parts

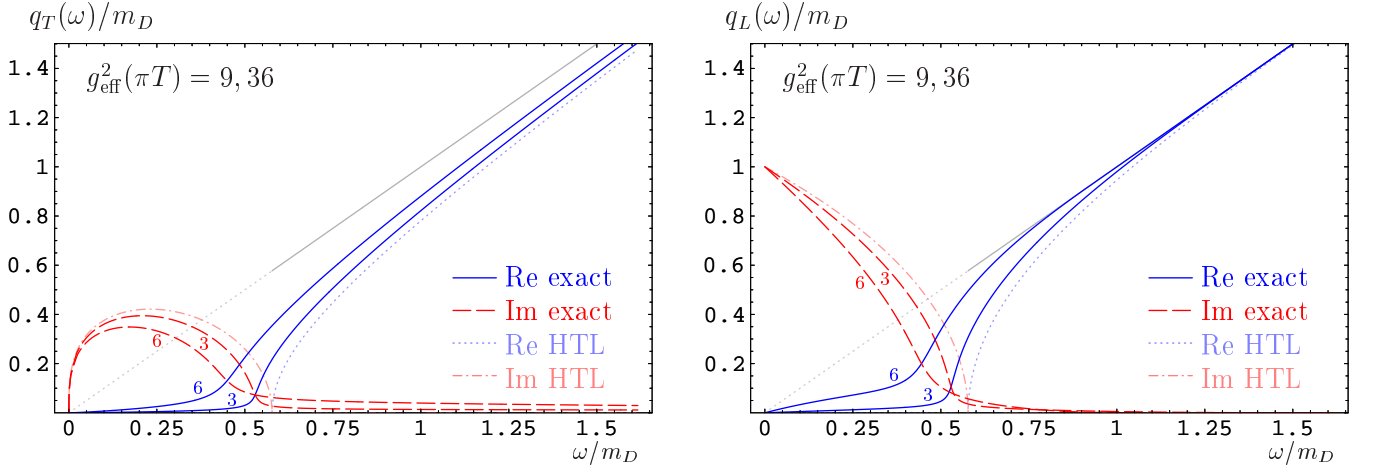


Figure 8: Real and imaginary part of the dispersion relation $q(\omega)$ as a function of real ω for $g_{\text{eff}}^2 = 9$ and 36 (labeled in the plot as 3 and 6 respectively for g_{eff}) in the large- N_f limit compared to the HTL result. The left panel shows the dispersion relation for the transverse component $q_T(\omega)$, while the right panel shows the longitudinal contribution $q_L(\omega)$. The exact large- N_f result is scaled by the large- N_f Debye mass m_D while the HTL result is scaled by the HTL Debye mass \hat{m}_D . Notably, the real part of $q(\omega)$ vanishes in the static case $\omega \rightarrow 0$ in the large- N_f limit also for larger couplings g_{eff}^2 , and one can see from the right panel that the Debye mass stays a real quantity even beyond HTL.

of transverse and longitudinal contributions coincide.⁴ The unique plasma frequency at $q = 0$ evolves according to Fig. 5.

Instead of assuming real wave vectors q and solving numerically for complex $\omega(q)$ as we had done in Fig. 6, we could start from a given real frequency ω and calculate the corresponding complex wave vector $q(\omega)$. This corresponds to calculating the linear response to perturbations with a given real frequency. The result is shown in Figure 8 for two different couplings $g_{\text{eff}}^2(\bar{\mu}_{\overline{\text{MS}}}) = 9$ and 36 (which are labelled as $g_{\text{eff}} = 3$ and 6 respectively in the plot). Above the plasma frequency, one has weakly damped spatial oscillations, and below the plasma frequency there is predominantly exponential screening, modulated by comparatively long-range oscillations that are absent in the HTL case (though fundamentally different from the Friedel oscillations [29, 30] we shall discuss further below). Following the curves down to vanishing frequency $\omega \rightarrow 0$ leads to the (real) value of the Debye mass in the longitudinal mode (right panel of Fig. 8), and in the transverse mode (left panel) to unscreened static modes (but significant dynamical screening at small but non-vanishing ω). The real part of $q(\omega)$, which corresponds to spatial oscillations, vanishes for both transverse and longitudinal modes, in the static limit $\omega \rightarrow 0$. The imaginary part of the longitudinal modes for $g_{\text{eff}} = 3, 6$, and HTL, approaches the value 1 in the static case as the curves are normalized to this value. The HTL results of Fig. 8, which are given by dotted and dash-dotted lines, are of course independent of the coupling in units of the HTL Debye mass. In a proper comparison between large N_f and HTL one should keep the renormalization scale dependence of m_D/\hat{m}_D from Fig. 4 in mind.

Figures 9 and 10 show the spectral functions at two different values of q/m_D . The combination $T^2 g_{\text{eff}}^2 \rho(\omega, q)$ on the ordinate is chosen in order to show a renormalization scale independent result: The quantity $g_{\text{eff}}^2 G$ is renormalization scale independent, which can be seen by combining Equations (2) and (11). In all four plots the broadening of the propagating mode peak with increasing coupling is evident. For the smaller wave vector $q/m_D = 0.2$ in Fig. 10, one furthermore nicely observes the decrease of the plasma frequency with increasing coupling. The HTL pole corresponds to a delta function peak, indicated by the vertical line.

⁴ This is due to the isotropy of the plasma. See Ref. [28] for counterexamples in anisotropic plasmas within the hard-loop approximation.

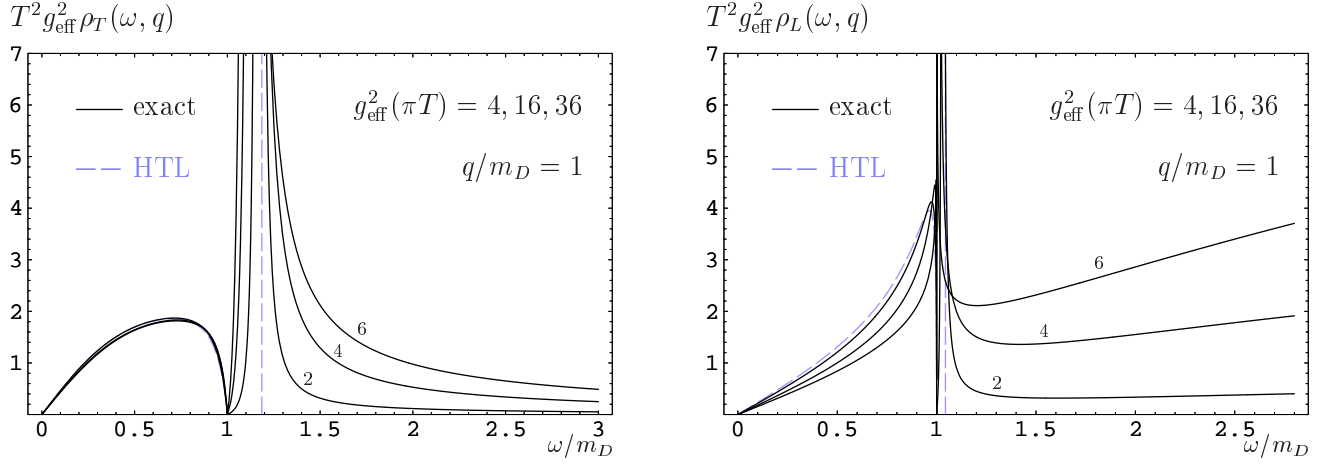


Figure 9: Spectral function ρ_T and ρ_L as a function of ω/m_D for $q/m_D = 1$ for various couplings $g_{\text{eff}}^2(\bar{\mu}_{\overline{\text{MS}}} = \pi T)$ (the lines in the plot are labelled by the values for $g_{\text{eff}} = 2, 4, 6$). As mentioned in the text, $g_{\text{eff}}^2 \rho(\omega, q)$ is a renormalization scale independent quantity, and $T^2 g_{\text{eff}}^2$ scales like \hat{m}_D^2 such that the HTL results for various couplings lie on top of each other. The position of the infinitely narrow HTL δ -peak is indicated by the vertical line, while the peaks at large N_f have a finite width and are shifted to lower energies with increasing coupling.

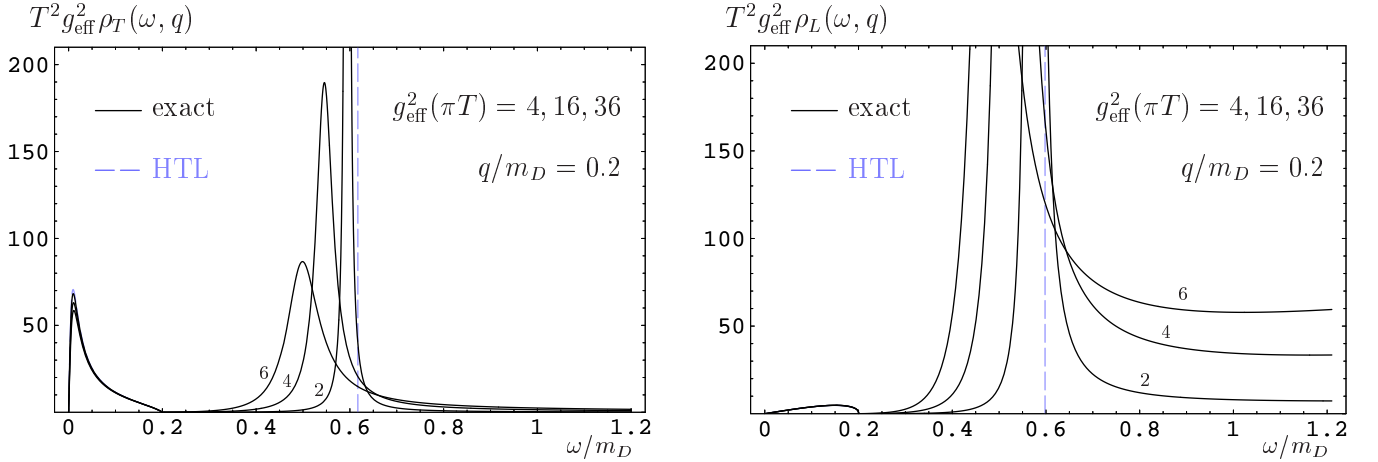


Figure 10: Same as figure (9) for $q/m_D = 0.2$. Due to the imaginary part of the plasma frequency, the peak of the propagating modes broadens. Additionally their frequency lowers.

B. Dispersion relations at finite chemical potential

In the following, we extend the analysis to finite chemical potential μ and zero temperature. Figure 11 shows the corresponding Debye mass. Here the prescription of fastest apparent convergence gives

$$\text{FAC-m} = 2\sqrt{e}\mu \approx 3.2974\mu \quad \text{at } T \rightarrow 0.$$

The FAC-m scale for arbitrary finite T and μ can be found in Ref. [31]. In addition to multiples of the FAC-m scale, also the simple scale choice $\bar{\mu}_{\overline{\text{MS}}} = 2\mu$, varied within a factor of 4, is depicted.

For the propagating modes, Figure 12 shows the imaginary part of the dispersion relations at zero temperature for the two couplings $g_{\text{eff}}^2 = 9$ and 36 at the scale $\bar{\mu}_{\overline{\text{MS}}} = 4\mu$. We did not plot the real part of the function separately, since they are almost indistinguishable from Figures 6 and 7 at zero chemical potential. The HDL result for the imaginary part in Fig. 12 is just zero, and the resulting imaginary part beyond HDL shows a threshold around the Fermi momentum $q \gtrsim \mu$ which can be explained as follows.

The process responsible for the imaginary part of the self-energy and thus for the propagator pole is the pair creation

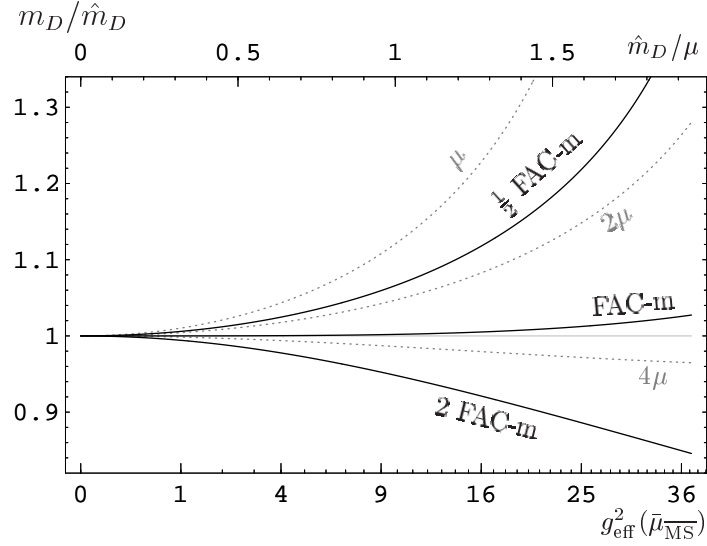


Figure 11: Comparison of the large- N_f Debye mass m_D to the corresponding HDL value \hat{m}_D at finite chemical potential and zero temperature. The FAC-m scale takes the value $\bar{\mu}_{\overline{\text{MS}}} = 2\sqrt{e}\mu$, and is varied by a factor of 4 in the plot. For comparison, also the scales $\bar{\mu}_{\overline{\text{MS}}} = \mu$, 2μ , and 4μ are displayed. The full Debye mass is in remarkable agreement with the HDL result for the FAC-m scale.

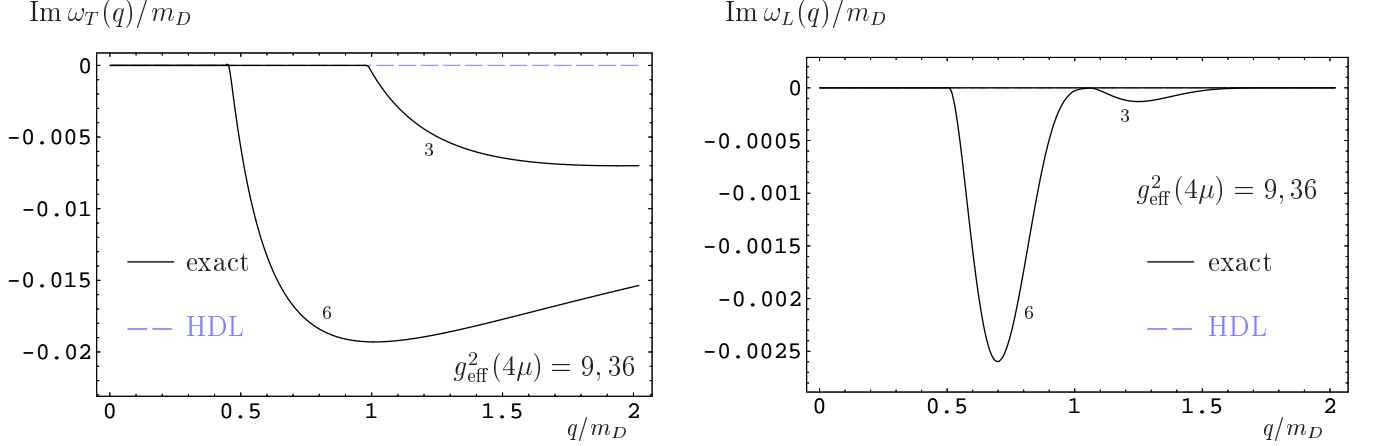


Figure 12: Imaginary part of the dispersion relation $\omega(q)$ at $T = 0$ as a function of real q for $g_{\text{eff}}^2(\bar{\mu}_{\overline{\text{MS}}} = 4\mu) = 9$ and 36 in the large- N_f limit compared to the HDL result. In contrast to the imaginary part at zero chemical potential in Figures 6 and 7, the imaginary part is zero up to a threshold $q \geq 2\mu - \text{Re}\omega(q)$ as explained in the text. The constant HDL line in the right panel is hidden by the exact large- N_f lines. The real part of the dispersion relations looks almost identical to the case of zero chemical potential (Figures 6 and 7) and is not plotted separately.

as shown in Figure 13. At real momenta q we are looking at time-like momenta for which the Landau damping process is kinematically forbidden, even for massive quarks. The only process that could contribute to the imaginary part of the self-energy is the creation of a quark with momentum $\mathbf{p} + \mathbf{q}$ and an anti-quark with momentum \mathbf{p} . At finite chemical potential, this process is kinematically restricted as the Fermi sea is filled up to the Fermi energy $E_F = \mu$ and the newly produced quark must have an energy above, $\epsilon_{\mathbf{p}+\mathbf{q}} \geq \mu$. The anti-quark can in principle be produced within the Fermi sea, $\epsilon_{\mathbf{p}} \geq 0$, but the dispersion relation of the gluon $\omega(q)$ dictates a minimal energy. From energy conservation of the process $\omega = \epsilon_{\mathbf{p}} + \epsilon_{\mathbf{p}+\mathbf{q}}$ we obtain for the angle θ between \mathbf{p} and \mathbf{q}

$$\cos \theta = \frac{\omega^2 - q^2 - 2\omega\epsilon_{\mathbf{p}}}{2pq}. \quad (26)$$

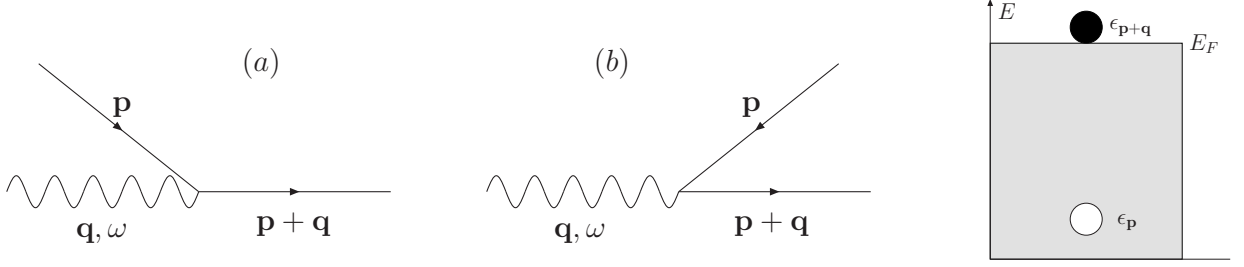


Figure 13: Diagrammatic processes (a) for Landau damping and (b) for gluon decay. Only the latter one is allowed kinematically for time-like gluons with $\omega^2 > q^2$. For non-zero chemical potential and zero temperature, this process is further restricted to $\omega + q \geq 2\mu$ as explained in the text. At the threshold, a quark with Fermi energy μ and a collinear anti-quark with energy $\epsilon_p = (\omega - q)/2$ are produced.

For zero mass, requiring a valid angle $-1 \leq \cos \theta \leq 1$, we obtain the kinematical restriction $\omega + q \geq 2p \geq \omega - q$. For a small finite quark mass $m^2 \leq Q^2 = \omega^2 - q^2$, the lower bound for p yields

$$p \geq \frac{1}{2} (\omega \gamma(Q) - q) \quad (27)$$

with $\gamma(Q) \equiv \sqrt{1 - 4m^2/Q^2}$. From the energy threshold of the quark $\epsilon_{p+q} \geq \mu$ we immediately obtain

$$\omega \gamma(Q) + q \geq 2\mu, \quad (28)$$

where $\gamma(Q) = 1$ in the massless case. The momentum thresholds in Figure 12 just follow this formula $q \geq 2\mu - \text{Re} \omega(q)$, scaled by the Debye mass m_D , where real part of $\omega(q)$ can be read off from Figures 6 and 7. It also explains why the momentum threshold for transverse modes is slightly lower than for the corresponding longitudinal mode, because $\omega_T(q) > \omega_L(q)$ for $q > 0$.

C. Friedel oscillations

For finite chemical potential and comparatively small temperatures, electrostatic screening at sufficiently large distances is no longer given by a simple Yukawa-type potential involving the Debye mass m_D . As is well known in nonrelativistic quantum many-body theory [29], the sharpness of the Fermi surface leads to an asymptotic behavior of the potential that is governed by so-called Friedel oscillations, implying a shell-like structure with alternating screening and overscreening. At $T = 0$, the amplitude of these oscillations decays by a power law and not like an exponential. As has been shown in Ref. [30], a similar modification of Debye screening occurs in high-density QED and QCD. In the following we shall investigate this effect quantitatively in the large- N_f theory.

The free energy of two (Abelian) static charges at a distance r is given by the Fourier transform of the electrostatic gauge boson propagator [30]

$$V(r) = Q_1 Q_2 \int \frac{d^3 k}{(2\pi)^3} e^{ik \cdot r} \frac{1}{k^2 + \Pi_L(k_0 = 0, k)}. \quad (29)$$

The deviation from Coulomb law behavior is described by the screening function

$$s(r) = \frac{4\pi r V(r)}{Q_1 Q_2} = \frac{1}{\pi} \text{Im} \int_{-\infty}^{\infty} \frac{dk k e^{ikr}}{k^2 + \Pi_L(k_0 = 0, k)}, \quad (30)$$

where we have used the fact that $\Pi_L(k_0 = 0, k)$ is an even function of $k = \sqrt{k^2}$. In the HTL approximation, where $\Pi_L(k_0 = 0, k) = \hat{m}_D^2$, one has simply $s(r) = e^{-m_D r}$.

However, as can be seen from the analytical results in Appendix B4, the full gauge boson propagator at zero temperature also involves logarithmic branch cuts which touch the real axis at momenta $k = \pm 2\mu$. Following Refs. [29, 30], we separate these branch cuts infinitesimally according to $k = \pm 2\mu \pm i\epsilon$ so that the integration path of Eq. (30) is threaded through the four branch points as shown in Fig. 14. Ignoring (as implicitly done in Ref. [30]) the Landau poles located at real $k = \pm \Lambda_L \gg \mu$ by moving them slightly into the lower half-plane, the screening function receives

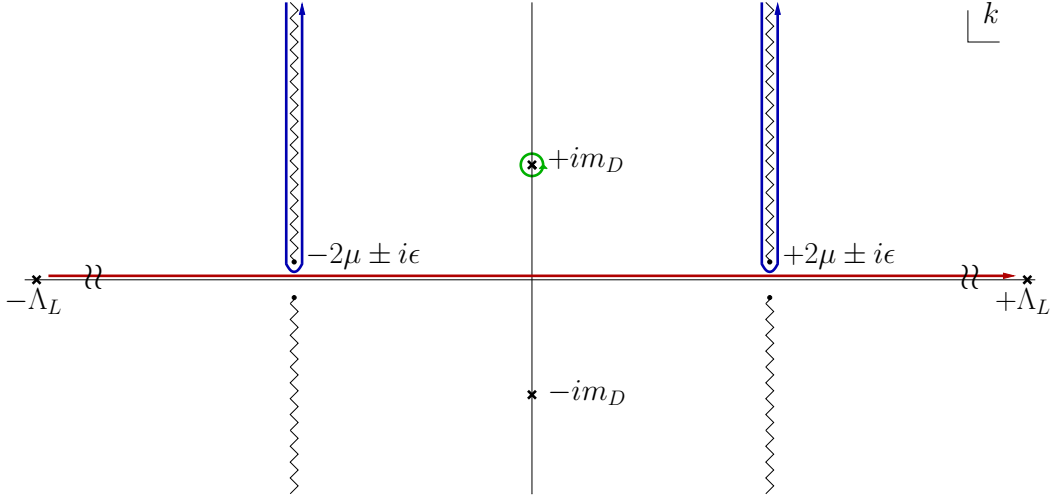


Figure 14: Analytic structure of the electrostatic propagator at zero temperature and integration paths for the screening function (30). If the Landau poles at real $k = \pm\Lambda_L$ are moved infinitesimally into the lower half-plane, the integration over the real k axis can be deformed to encircle the two branch cuts starting at $k = \pm 2\mu + i\epsilon$ and the Debye mass pole at $k = im_D$.

contributions from the Debye mass pole at $k = im_D$ and two integrations along the cuts starting at $k = \pm 2\mu + i\epsilon$. Because of the latter, the electrical screening at sufficiently large distances is dominated by oscillatory behavior with wavelength π/μ . In the ultrarelativistic case the asymptotic behavior has been calculated in Ref. [30] with the result

$$\lim_{r \rightarrow \infty} s(r) = \frac{g_{\text{eff}}^2}{16\pi^2} \left[1 + \frac{g_{\text{eff}}^2}{6\pi^2} \left(\ln \frac{\bar{\mu}_{\overline{\text{MS}}}}{4\mu} + \frac{11}{6} \right) \right]^{-2} \frac{\sin(2\mu r)}{(\mu r)^3}, \quad (31)$$

which we have transcribed to the $\overline{\text{MS}}$ scheme that we are using here. Nonzero temperature moves the branch cuts away from the real axis, leading to an extra exponential suppression factor [30] $e^{-2\pi T r}$ so that they cease to govern the asymptotic behavior for $T \gtrsim m_D/(2\pi)$. We shall therefore concentrate on the $T = 0$ case, where Friedel oscillations should be maximally important.

With regard to potential implications to high-density QED or QCD [30], it is of interest to know whether deviations from standard Debye screening occur already at moderate distances before the screening function has become negligibly small. This requires a numerical evaluation of the integral in Eq. (30) and the results for $g_{\text{eff}}^2 = 9$ and $g_{\text{eff}}^2 = 16$ are shown in Fig. 15. The dotted line shows the contribution from the Debye mass pole with values $m_D = 0.94269\mu$ and $m_D = 1.24705\mu$, respectively; the long-dashed lines labelled “Friedel” correspond to the asymptotic formula (31). The full large- N_f result which excludes contributions from the Landau poles by moving them infinitesimally into the lower half-plane is given by the line labelled “exact”. As one can see, significant deviations from Debye screening appear only at such large distances that the screening function $s(r)$ is of the order 10^{-4} or below for $g_{\text{eff}}^2 = 9$ and $g_{\text{eff}}^2 = 16$. At these couplings, the Landau pole is at scales of the order of $10^4\mu$ and $3 \times 10^2\mu$, respectively. If instead of circumventing the Landau pole we cut off the momentum integration at $a\Lambda_L$ with a varied between $1/2$ and $1/\sqrt{2}$, this affects the screening function already considerably above the scale where Friedel oscillations occur, as shown by the dash-dotted lines in Fig. 15.⁵ In real QCD, the one-loop Dyson-resummed gluon propagator also involves vacuum contributions from the gluon loop which gives asymptotic freedom and eliminates the Landau pole.⁶ Because of this, the results obtained by simply circumventing the Landau pole in the large- N_f theory are probably a reasonable model of screening in high-density QCD at low temperature. Taken as such, these results suggest that Friedel oscillations occur only at distances where the screened potential is already very small. At low but nonzero temperature, the importance of Friedel oscillations is further reduced by an extra exponential suppression factor [30] $e^{-2\pi T r}$ until they disappear completely for $T \gtrsim m_D/(2\pi)$.

⁵ A cutoff independent of r actually would give rapid oscillations at large distances. In Fig. 15 we have instead pinned the cutoff to the last zero of the oscillatory integrand below $a\Lambda_L$.

⁶ It also introduces a branch cut lying on the imaginary axis, which is however not stable against higher-order contributions.

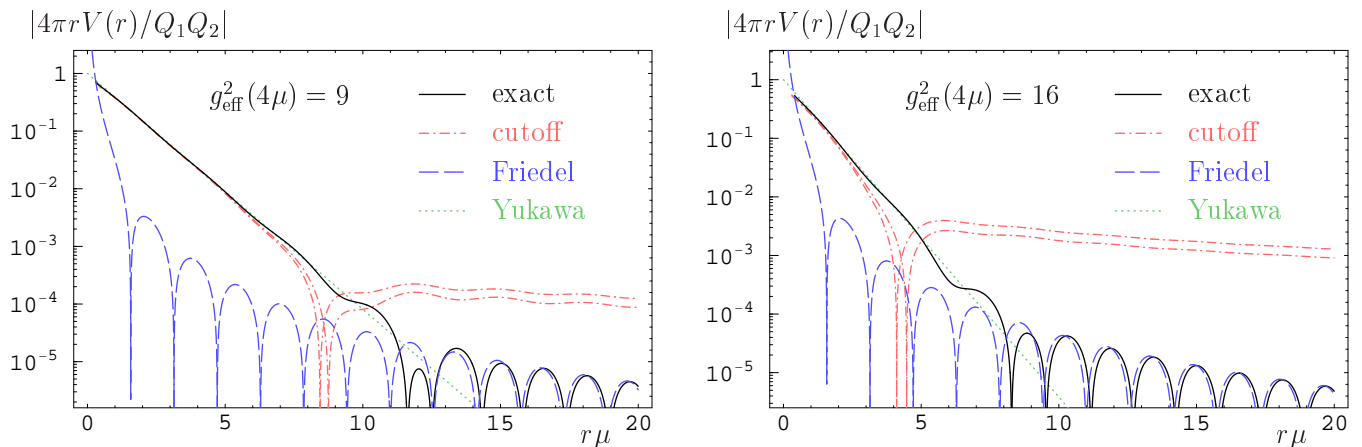


Figure 15: Electrostatic screening in the large- N_f theory at $T = 0$ for effective coupling $g_{\text{eff}}^2(\bar{\mu}_{\overline{\text{MS}}}=4\mu) = 9$ and 16 . The full line labelled “exact” shows the numerical result obtained by circumventing the Landau pole in the upper half-plane (see Fig. 14); the lines labelled “cutoff” correspond to cutoffs at the last zero of the integrand in (30) below $|k| = a\Lambda_L$ with $a = 1/2 \dots 1/\sqrt{2}$. The dotted line labelled “Yukawa” corresponds to an exponential with exact large- N_f screening mass $m_D(g_{\text{eff}})$, the long-dashed line labelled “Friedel” represents the asymptotic formula (31).

In ultrarelativistic (massless) QED, where $g_{\text{eff}}^2 \approx 0.092$, Friedel oscillations are much more suppressed than in the examples above. Ordinary Debye screening dominates out to distances $r \sim 250\mu^{-1}$, where the screening function $s \lesssim 10^{-10}$. However, Friedel oscillations in massive QED are less strongly suppressed – they then come with an extra factor of mr in the screening function [29, 30]. Indeed, Friedel oscillations have been seen experimentally in the nonrelativistic electron gas.

V. CONCLUSIONS

In this paper we studied the spectral functions and dispersion relations of the gauge boson propagator in the large- N_f limit. This allows us to investigate the properties of this propagator not only in the weak coupling regime around $g_{\text{eff}}^2(\pi T) \lesssim 4$, but also in the strong coupling regime $4 \lesssim g_{\text{eff}}^2(\pi T) \lesssim 36$, where strict perturbation theory fails but the influence of the Landau pole is still negligible. For larger values of the coupling, the usual spectral function sum rules have to be corrected due to the presence of the Landau pole.

Numerically we calculated the Debye mass, the plasma frequency, dispersion relations, and spectral functions at finite temperature and compared those to the analytically known HTL results. The poles of the propagators at large N_f are renormalization scale independent. Depending on their vicinity to the real energy axis, they appear as peaks of finite width in the spectral functions. These poles do not lie on the physical sheet of the propagator, so a proper analytic continuation of the self-energies into the neighbouring unphysical sheet is necessary. In addition to moving the branch cuts of the logarithms involved as it is sufficient for the vacuum piece of the self-energy, one also has to adjust the integration path of a numerical integration appearing within the thermal piece of the self-energy in order to avoid a crossing with logarithmic singularities or branch cuts.

In the large- N_f limit, the full Debye mass is remarkably close to the HTL value for renormalization scale $\bar{\mu}_{\overline{\text{MS}}} \approx \mu T$ even up to extremely large couplings. The plasma frequency, and to lesser degree the frequency of the propagating modes, acquire an imaginary part which is caused by the vacuum process of quark-antiquark pair creation neglected in the HTL approximation. The peaks in the spectral functions get broader with increasing coupling and their frequency relative to the HTL value decreases. Overall, there do not seem to be significant qualitative changes in the gauge boson propagator as one increases the coupling from small to rather large values. By contrast, the interaction pressure of the large- N_f theory exhibits nonmonotonic behavior. As will be shown in a subsequent paper [15], the latter can be better understood in terms of the entropy. While the nontrivial content of the large- N_f pressure can be formulated entirely in terms of the gauge boson propagator, a quasiparticle analysis of the entropy shows that the bosonic contribution is unsurprising, whereas the fermionic contributions involve next-to-leading order results for the asymptotic quark mass which accounts for the nonmonotonic behavior at large coupling.

We have also investigated quantitatively the effect of asymptotic Friedel oscillations in electrostatic screening at zero temperature and high chemical potential with negligible fermion mass. While Friedel oscillations are a truly tiny

effect in ultrarelativistic (massless) QED, their importance increases with effective coupling strength. However, the potential of static charges remains dominated by Yukawa-like Debye screening up to distances where the screening function has dropped by several orders of magnitude and where the effect of a cutoff to remove the Landau pole would be of comparable or greater importance.

Acknowledgments

The numerical integration paths have mostly been drawn with the packages AXODRAW [32] and JAXODRAW [33].

Appendix A: BOSONIC ONE-LOOP SELF-ENERGY

1. Full one-loop result at zero mass

The vacuum part of the bosonic self energy in the Feynman gauge (covariant gauge with gauge parameter $\alpha = 1$) for N_f flavors and N_c colors, coupling $\alpha_s = g^2/(4\pi)$, and the renormalization scale $\bar{\mu}_{\overline{\text{MS}}}$ in the modified minimal subtraction ($\overline{\text{MS}}$) scheme is given by

$$\Pi_{\text{vac}}(Q) = \frac{g^2}{16\pi^2} Q^2 \left\{ \frac{2N_f - 5N_c}{3} \left[\log \left(\frac{-Q^2}{\bar{\mu}_{\overline{\text{MS}}}^2} \right) - \frac{5}{3} \right] + \frac{2}{3} N_c \right\}. \quad (\text{A1})$$

The thermal part of the bosonic self energy reads [4]

$$\Pi_{\text{L,th}}(q_0, q) = g^2 (N_f H_f + N_c H_b), \quad (\text{A2})$$

$$\Pi_{\text{T,th}}(q_0, q) = \frac{g^2}{2} \left(-\frac{q^2 - q_0^2}{q^2} (N_f H_f + N_c H_b) + (N_f G_f + N_c G_b) \right), \quad (\text{A3})$$

for N_f flavors and N_c colors, where the fermionic functions G_f and H_f can be written as one-dimensional integrals

$$G_f = \frac{1}{2\pi^2} \int_0^\infty dk n_f(k) \left(4k - \frac{q^2 - q_0^2}{2q} L_1 \right), \quad (\text{A4})$$

$$H_f = \frac{1}{2\pi^2} \int_0^\infty dk n_f(k) \left(2k - \frac{q^2 - q_0^2 - 4k^2}{4q} L_1 - q_0 k L_2 \right), \quad (\text{A5})$$

and similarly the bosonic functions G_b and H_b

$$G_b = \frac{1}{2\pi^2} \int_0^\infty dk n_b(k) \left(4k - \frac{5}{4} \frac{q^2 - q_0^2}{q} L_1 \right), \quad (\text{A6})$$

$$H_b = \frac{1}{2\pi^2} \int_0^\infty dk n_b(k) \left(2k - \frac{2q^2 - q_0^2 - 4k^2}{4q} L_1 - q_0 k L_2 \right), \quad (\text{A7})$$

with

$$L_1 = \log \left(\frac{2k + q - q_0}{2k - q - q_0} \right) - \log \left(\frac{2k - q + q_0}{2k + q + q_0} \right), \quad (\text{A8})$$

$$L_2 = \log \left(\frac{2k + q - q_0}{2k - q - q_0} \right) - 2 \log \left(\frac{-q + q_0}{q + q_0} \right) + \log \left(\frac{2k - q + q_0}{2k + q + q_0} \right), \quad (\text{A9})$$

and the bosonic and fermionic distribution functions at temperature T and chemical potential μ

$$n_b(k) = \frac{1}{e^{k/T} - 1}, \quad (\text{A10})$$

$$n_f(k) = \frac{1}{2} \left(\frac{1}{e^{(k-\mu)/T} + 1} + \frac{1}{e^{(k+\mu)/T} + 1} \right). \quad (\text{A11})$$

These expressions are valid for all complex q_0 in a rotation from Euclidean space $q_0 = i\omega$ to Minkowski space $q_0 = \omega + i\epsilon$ with $\epsilon > 0$. For the analytic continuation into the region with $\epsilon < 0$ the expressions L_1 and L_2 have to be changed as described below.

Apart from their HTL/HDL content, the bosonic contributions (A6) and (A7) are gauge dependent (see Refs. [34, 35] for one-loop results in gauges other than Feynman).

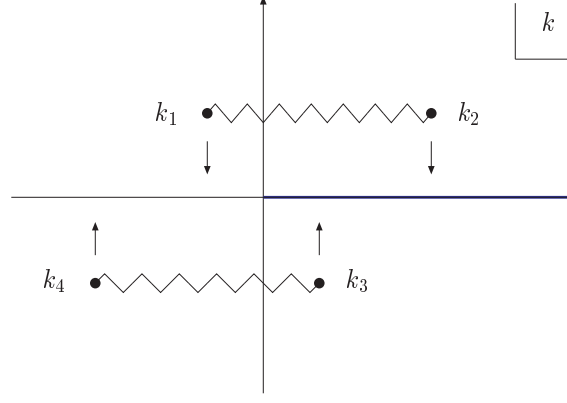


Figure 16: Branch cut and singularity structure of the initial integrand for G_f , Eq. (A4), for complex k . The singular points k_1 to k_4 correspond to solutions of $2k \pm q \pm q_0 = 0$ from the logarithmic argument in L_1 , Eq. (A8), which are pairwise connected by logarithmic branch cuts. For $q_0 = \omega + i\epsilon$, all four singularities will simultaneously cross the real k axis as ϵ changes from positive to negative sign.

2. HTL and HDL

The corresponding HTL or HDL expressions can be extracted by demanding that the external momenta q_0 and q be small compared to temperature T and/or chemical potential μ (that is to take the leading contribution in a $1/k$ expansion of the integrand, since the main contribution is expected to come from large loop momenta k). The relevant physical scale is then given by the HTL Debye mass (HTL quantities are marked by a $\hat{\cdot}$)

$$\hat{m}_D^2 = g^2 \left\{ \frac{2N_c + N_f}{6} T^2 + N_f \frac{\mu^2}{2\pi^2} \right\}. \quad (\text{A12})$$

In this limit, the equations (A4) to (A7) reduce to

$$\hat{G}_f = \frac{T^2}{6} + \frac{\mu^2}{2\pi^2}, \quad (\text{A13})$$

$$\hat{H}_f = \left(\frac{T^2}{6} + \frac{\mu^2}{2\pi^2} \right) \left\{ 1 + \frac{q_0}{2q} \log \left(\frac{-q + q_0}{q + q_0} \right) \right\}, \quad (\text{A14})$$

$$\hat{G}_b = \frac{T^2}{3}, \quad (\text{A15})$$

$$\hat{H}_b = \frac{T^2}{3} \left\{ 1 + \frac{q_0}{2q} \log \left(\frac{-q + q_0}{q + q_0} \right) \right\}. \quad (\text{A16})$$

In the zero temperature limit \hat{G}_b and \hat{H}_b vanish.

Appendix B: ANALYTIC CONTINUATION OF THE SELF-ENERGY

1. Integration in the complex k plane

The k -integration in the self-energy expressions for $G_{f,b}$ and $H_{f,b}$ in equations (A4) to (A7) runs over real k only. One might assume that for the analytic continuation of those functions it is sufficient to take care of the logarithms appearing in L_1 and L_2 and leave the real k integration untouched. It turns out that this simple approach fails. For continuing the functions properly in the complex domain, we should think of the k -integration as an analytic integration in the complex k plane. L_1 and L_2 provide singular points and branch cuts in the complex k plane that move around, as ϵ varies. As long as the logarithmic singularities or branch cuts never touch the integration line, the resulting integral is an analytic, complex function. We will demonstrate the necessary procedure for the branch cut structure of L_1 of G_f , but the following considerations can be readily applied to L_2 and therefore to G_b , H_f , and H_b .

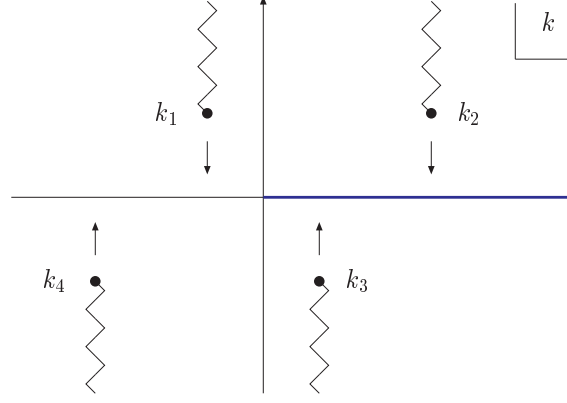


Figure 17: First we break up the branch cuts according to Eq. (B2).

Figure 16 shows the singularity and branch cut structure for the integrand of G_f , Eq. (A4), which is determined for complex k by the logarithms in L_1 , Eq. (A8). For $q_0 = \omega + i\epsilon$, the logarithmic singularities lie at

$$\begin{aligned} k_1 &= \frac{1}{2}(-q + \omega + i\epsilon), \\ k_2 &= \frac{1}{2}(q + \omega + i\epsilon), \\ k_3 &= \frac{1}{2}(q - \omega - i\epsilon) = -k_1, \\ k_4 &= \frac{1}{2}(-q - \omega - i\epsilon) = -k_2, \end{aligned} \tag{B1}$$

so with $\epsilon > 0$ and real q and ω we find that k_1 and k_2 lie initially above the real k axis, while k_3 and k_4 lie below. The branch cut structure shown in Figure 16 corresponds to the initial formula for L_1 from Eq. (A8): k_1 and k_2 are connected by a logarithmic branch cut, as are k_3 and k_4 . The problem is evident as we try to analytically extend the integration from the region $\epsilon > 0$ to $\epsilon < 0$: All four singularities will pass the real axis at the same time, as do the corresponding branch cuts that penetrate each other. How can we choose an integration path that avoids contact with these singularities and branch cuts? The solution lies in the fact that we can move around the branch cuts.

First we break up the branch cuts from the logarithmic expressions in L_1 and L_2 as shown in Figure 17. Using the logarithmic functions $\log^\uparrow(z)$ and $\log^\downarrow(z)$ from Eqs. (8) and (9) with branch cuts along the positive or negative imaginary axis, we can rewrite equation (A8) as

$$\begin{aligned} L_1^{\text{break-up}} &= \log^\uparrow(2k + q - q_0) - \log^\uparrow(2k - q - q_0) \\ &\quad - \log^\downarrow(2k - q + q_0) + \log^\downarrow(2k + q + q_0), \end{aligned} \tag{B2}$$

which agrees with L_1 on the real k axis, and similarly for L_2

$$\begin{aligned} L_2^{\text{break-up}} &= \log^\uparrow(2k + q - q_0) - \log^\uparrow(2k - q - q_0) \\ &\quad - 2 \left(\log^\downarrow(-q + q_0) - \log^\downarrow(q + q_0) \right) \\ &\quad + \log^\downarrow(2k - q + q_0) - \log^\downarrow(2k + q + q_0). \end{aligned} \tag{B3}$$

The branch cuts in the two logarithmic expressions of L_2 independent of k (second line) are chosen such that the functions continue analytically for real q and ω when ϵ changes its sign from positive to negative. Using $L_1^{\text{break-up}}$ gives the branch cut structure as shown in Figure 17. It is now clear how the path should be deformed from $\epsilon > 0$ in Fig. 17 to $\epsilon < 0$ in Fig. 18. To further justify this procedure, let us note that one could have used the new integration path from Fig. 18 already in Fig. 17, where it would not have changed the result of the integration, as the result of the complex integration is of course path independent. Keeping the same S-shaped integration path in both figures, it is clear that moving a logarithmic singularity across the real k axis is not different from moving it around anywhere else in the complex k plane, provided no singularities are crossed.

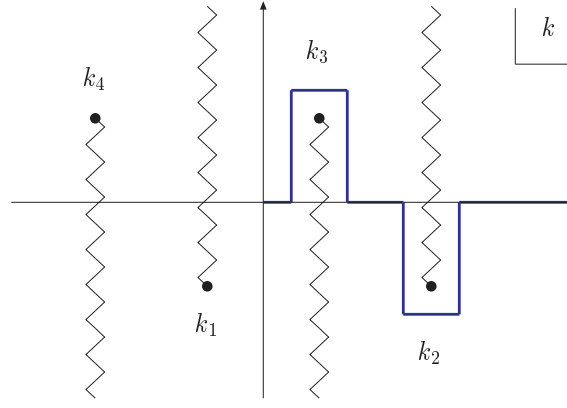


Figure 18: In this way, we can deform the integration path when the singularities and branch cuts move across the real k axis. Note that we could have used this integration path already in figure 17. In that case it is obvious that moving the singularities across the real k axis would not be different from moving the singularities around anywhere else in the complex k plane.

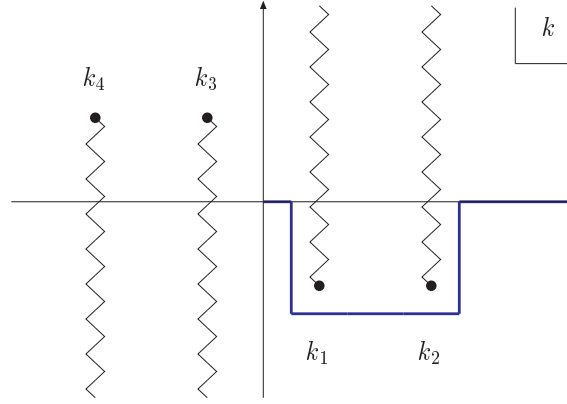


Figure 19: If $\text{Re } k_1 > 0$ and $\text{Re } k_3 < 0$ then the path would look like this. In Figures 16 to 18 we had assumed $\text{Re } k_3 > 0$ and $\text{Re } k_1 < 0$.

Practically, to change from positive to negative ϵ , we could either literally choose a numerical integration contour similar to Figure 18, or we could basically stick to the original integration along the real k axis, taking correcting branch cut contributions from the real axis to, say, k_2 and k_4 into account. At first sight, the latter strategy seems insofar appealing, as the branch-cut contributions can be calculated analytically without the necessity of numerical integration. This strategy is briefly discussed below in Appendix B 3. But since the integration parts along the real k axis have to be integrated numerically anyway, it turns out to be easier to choose an appropriate integration path for numerical integration in the complex k plane which avoids all branch cuts in a safe distance.

2. Choosing a complex integration path

We shall show how to choose an integration path in the complex k plane that circumvents the branch cuts. In choosing the path, we only need to care about logarithmic singularities k_i with positive real part as only those will cross the initial integration range $k \in [0, \infty)$. Assuming that $\text{Re } q > 0$ and real $\omega > 0$ in $q_0 = \omega + i\epsilon$, we see that in (B1) the singularity $\text{Re } k_2 > 0$ always lies in the right half of the complex plane while $\text{Re } k_4 < 0$ lies on the left half. Also k_1 and k_3 lie on opposite sides of the imaginary k -axis, so there are two distinct cases for the path topology: Either $\text{Re } k_1 > 0$ as in figure 19, or $\text{Re } k_3 > 0$ as in figure 18. In the latter case, $\text{Re } k_3$ is always smaller than $\text{Re } k_2$, but in the former case $\text{Re } k_1$ could be either smaller or larger than $\text{Re } k_2$.

At finite chemical potential the fermionic distribution function $n_f(k)$ from Eq. (A11) provides additional poles at $k = \pm\mu + (2n+1)i\pi T$ ($n \in \mathbb{Z}$). Figure 20 shows the particular case $0 < \text{Re } k_1 < \mu < \text{Re } k_2$, but the Matsubara

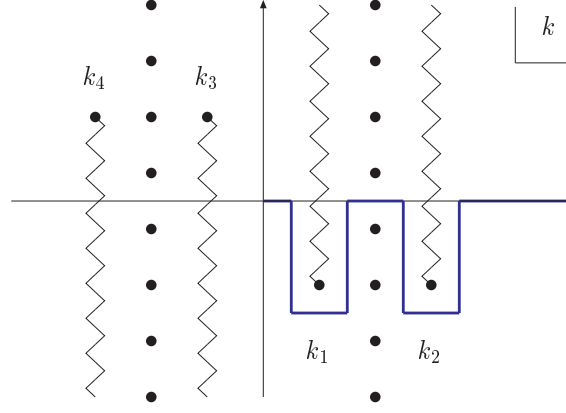


Figure 20: At finite chemical potential μ , the fermionic distribution function (A11) provides additional poles at the Matsubara frequencies $k = \pm\mu + (2n + 1)i\pi T$ ($n \in \mathbb{Z}$) which have to be avoided.

frequencies can also lie to the left of $\text{Re } k_1$ or to the right of $\text{Re } k_2$. As the initial path for the k -integration (starting from $\epsilon > 0$) lies along the real k axis between the poles $k = \mu \pm i\pi T$, also after the analytic continuation from $\epsilon > 0$ to $\epsilon < 0$ the integration path has to stay between these two lowest Matsubara frequency poles. Similarly, one has to take care of the Matsubara frequency poles in the case $\text{Re } k_3 > 0$ as in figure 18.

There is a lot of freedom in choosing an integration path that fulfills all of these constraints and correctly avoids the problematic regions in the complex plane. Our implementation of the complex integration path follows essentially those suggested in Figures 18, 19, and 20, where we vary the minimal distances to the branch cuts and singularities for testing purposes. One can readily check that the final result is independent of the exact implementation of a correct integration path.

The same integration path can be used for calculating the derivative with respect to q_0 , by forming the derivative of the integrand first. The derivative of the self-energy functions can be used in specifying the Jacobian for a numerical root search. The search for the Debye mass requires complex q . Assuming $\text{Re } q \geq 0$ and $\text{Im } q \geq 0$ this implies straightforward modifications to the integration paths: As the real part of $q(q_0)$ vanishes in the limit $q_0 \rightarrow 0$, basically k_1 and k_2 from Eqs. (B1) come to lie vertically aligned on top of each other in Fig. 19 instead of horizontally aligned side by side.

3. Alternative ways of calculating the analytic continuation

One possibility (which we did not follow in our numerical evaluation) is to analytically calculate the contribution caused by a branch cut that crosses our original integration line. Integrating a function $f(z) \log(z)$ (where $f(z)$ is analytic) around a part of the branch cut is equivalent to integrating $f(z)2\pi i$ along the path of the branch cut, e.g. with $a < b < 0$ we can write

$$\left[\int_{a-i\epsilon}^{b-i\epsilon} + \int_{b+i\epsilon}^{a+i\epsilon} \right] f(z) \log(z) dz = \int_b^a f(z) 2\pi i dz, \quad (\text{B4})$$

as the real parts of $\log(z) = \log|z| + i \arg z$ along the two contour parts cancel each other, while the net contribution comes from integrating $\pm i\pi$ along the contour.

For $G_{f,b}$ we basically have to integrate $n_{f,b}(k) \times \text{polynomial}(k) \times 2\pi i$. This can be done analytically. Here are some

examples for n_b

$$\int n_b(k)dk = T \log(e^{k/T} - 1) - k, \quad (\text{B5})$$

$$\int kn_b(k)dk = T^2 \text{Li}_2(e^{k/T}) + kT \log(1 - e^{k/T}) - \frac{k^2}{2}, \quad (\text{B6})$$

$$\begin{aligned} \int k^2 n_b(k)dk &= -2T^3 \text{Li}_3(e^{k/T}) + 2kT^2 \text{Li}_2(e^{k/T}) \\ &\quad + k^2 T \log(1 - e^{k/T}) - \frac{k^3}{3}, \end{aligned} \quad (\text{B7})$$

where $\text{Li}_n(z)$ is the polylogarithm function. Similar expressions can be derived for n_f . These functions have branch cuts for $\text{Re}(k) > 0$ which would have to be corrected, e.g.

$$\int n_b(k)dk = T \log(e^{k/T} - 1) - k - 2\pi i \left\lceil \frac{\text{Im}(k)}{2\pi T} - \frac{1}{2} \right\rceil, \quad (\text{B8})$$

where the ceiling function $\lceil x \rceil$ means the smallest integer $\geq x$. Similar adjustments would be necessary for the other relations above. Since these adjustments are error-prone, and we have to integrate a large part of the result numerically anyway, it turns out to be more straightforward to choose a complex integration path and integrate everything numerically, as described in the previous section.

Another possibility to obtain the analytically continued propagator is to exploit the relation between propagator and spectral function, Eq. (14). Apart from the fact that this would introduce another numerical integration over q_0 , this relation is only reliable for small couplings where the influence of the Landau pole can be neglected. For larger couplings, the correction term of Eq. (22) would have to be taken into account.

Yet another way to obtain the analytically continued retarded propagator is given by adding a correction term to the Feynman propagator (a detailed description of this procedure can be found in Appendix B of Ref. [36])

$$G^R(\omega - i\epsilon, q) = G(\omega - i\epsilon) + 2iI(\omega - i\epsilon, q). \quad (\text{B9})$$

Along the discontinuity, i.e. for real ω , the correction term coincides with the spectral function from Eq. (5), $I(\omega, q) = \rho(\omega, q)$, but different from the spectral function, the function $I(\omega - i\epsilon, q)$ has to be an analytic function. By the uniqueness theorem of the analytic continuation, one obtains the unique retarded Greens function $G^R(\omega - i\epsilon, q)$. The tricky point of this approach is to find the correct analytic continuation of the spectral function $\rho(q_0, q)$. We can not readily apply this method to the large- N_f limit, as the spectral function is, just like the propagator itself, only obtained numerically. The proper analytic continuation of the function $I(q_0, q)$ would be just as tough as the analytic continuation of $G(q_0, q)$ itself.

4. Analytic result at zero temperature and finite chemical potential

The fermionic distribution function (A11) can be expanded for small T as

$$\begin{aligned} n_f(k, T, \mu) &= \frac{1}{2} (\theta(-(k - \mu)) + \theta(-(k + \mu))) \\ &\quad + T^2 \frac{\pi^2}{12} (\delta'(k - \mu) + \delta'(k + \mu)) + O(T^4) \end{aligned} \quad (\text{B10})$$

where $\delta'(k - \mu)$ is to be understood in the sense of distributions

$$\int_{-\infty}^{\infty} \delta'(k - \mu) f(k) dk = -f'(\mu). \quad (\text{B11})$$

In this limit, the integrations in (A4) to (A7) can be performed analytically. The analytic continuation is straightforward with the tools presented here. The result at zero temperature [37] can be written using

$$R(q_0, q) = (2\mu + q_0 + q) \log(2\mu + q_0 + q) - (q_0 + q) \log(q_0 + q), \quad (\text{B12})$$

$$\begin{aligned} S(q_0, q) &= (2\mu + q_0 - 2q)(2\mu + q_0 + q)^2 \log(2\mu + q_0 + q) \\ &\quad - (q_0 - 2q)(q_0 + q)^2 \log(q_0 + q). \end{aligned} \quad (\text{B13})$$

We use the following abbreviation to keep a lot of terms in dense notation

$$R_{\pm}^{\pm}(q_0, q) \equiv R(q_0, q) - R(q_0, -q) + R(-q_0, q) - R(-q_0, -q) \quad (\text{B14})$$

and similarly for S_{\pm}^{\pm} (just replace R by S). The functions $G_f^{(0)}$ and $H_f^{(0)}$ (the upper index “(0)” denotes the $T = 0$ limit) can then be written as

$$G_f^{(0)}(q_0, q) = \frac{1}{2\pi^2} \left(\mu^2 + \frac{q_0^2 - q^2}{8q} R_{\pm}^{\pm}(q_0, q) \right), \quad (\text{B15})$$

$$H_f^{(0)}(q_0, q) = \frac{1}{96\pi^2} \left(32\mu^2 + \frac{1}{q} \left(-24\mu^2 q_0 (\log(q_0 + q) - \log(q_0 - q)) + S_{\pm}^{\pm}(q_0, q) \right) \right). \quad (\text{B16})$$

In order to correctly analytically continue these formulae into the region of $\epsilon < 0$, one needs to replace all logarithms that contain an initially positive (negative) q_0 to \log^{\downarrow} (\log^{\uparrow}) from equations (8) and (9). Defining $R^{\downarrow(\uparrow)}(q_0, q) := [R(q_0, q) \text{ with } \log \rightarrow \log^{\downarrow(\uparrow)}]$ and similarly for S , we can write

$$R_{\pm\uparrow}^{\pm\downarrow}(q_0, q) \equiv R^{\downarrow}(q_0, q) - R^{\downarrow}(q_0, -q) + R^{\uparrow}(-q_0, q) - R^{\uparrow}(-q_0, -q) \quad (\text{B17})$$

and the very same for S . The analytically continued functions $G_f^{(0)}$ and $H_f^{(0)}$ can then be written as

$$G_f^{(0)}(q_0, q) = \frac{1}{2\pi^2} \left(\mu^2 + \frac{q_0^2 - q^2}{8q} R_{\pm\uparrow}^{\pm\downarrow}(q_0, q) \right), \quad (\text{B18})$$

$$H_f^{(0)}(q_0, q) = \frac{1}{96\pi^2} \left(32\mu^2 + \frac{1}{q} \left(-24\mu^2 q_0 (\log^{\downarrow}(q_0 + q) - \log^{\downarrow}(q_0 - q)) + S_{\pm\uparrow}^{\pm\downarrow}(q_0, q) \right) \right). \quad (\text{B19})$$

The next term in the small T expansion of equation (B10) is easily calculated using (B11) and can be written as (the upper index “(2)” denotes the second derivative w.r.t. T at $T = 0$)

$$G_f^{(2)}(q_0, q) = \frac{1}{24} \frac{16\mu^2(4\mu^2 - 3q_0^2 - q^2)}{16\mu^4 - 8\mu^2(q_0^2 + q^2) + (q_0^2 - q^2)^2}, \quad (\text{B20})$$

$$H_f^{(2)}(q_0, q) = \frac{1}{24q} [(2\mu + q_0) (\log(2\mu + q + q_0) - \log(2\mu - q + q_0)) - 2q_0 (\log(q_0 + q) - \log(q_0 - q)) + (2\mu - q_0) (\log(2\mu + q - q_0) - \log(2\mu - q - q_0))]. \quad (\text{B21})$$

As $G_f^{(2)}$ is regular in the whole q_0 complex plane, we only have to take care of the proper analytic continuation of $H_f^{(2)}$:

$$H_f^{(2)}(q_0, q) = \frac{1}{24q} \left[(2\mu + q_0) (\log^{\downarrow}(2\mu + q + q_0) - \log^{\downarrow}(2\mu - q + q_0)) - 2q_0 (\log^{\downarrow}(q_0 + q) - \log^{\downarrow}(q_0 - q)) + (2\mu - q_0) (\log^{\uparrow}(2\mu + q - q_0) - \log^{\uparrow}(2\mu - q - q_0)) \right]. \quad (\text{B22})$$

The analytically continued expansion at small T and finite chemical potential is then given as

$$\begin{aligned} G_f(q_0, q) &= G_f^{(0)}(q_0, q) + T^2 G_f^{(2)}(q_0, q) + O(T^4), \\ H_f(q_0, q) &= H_f^{(0)}(q_0, q) + T^2 H_f^{(2)}(q_0, q) + O(T^4). \end{aligned}$$

[1] V. P. Silin, Sov. Phys. - JETP **11**, 1136 (1960).

[2] O. K. Kalashnikov and V. V. Klimov, Sov. J. Nucl. Phys. **31**, 699 (1980).

- [3] V. V. Klimov, Sov. J. Nucl. Phys. **33**, 934 (1981).
- [4] H. A. Weldon, Phys. Rev. **D26**, 1394 (1982).
- [5] H. A. Weldon, Phys. Rev. **D40**, 2410 (1989).
- [6] R. D. Pisarski, Nucl. Phys. **A498**, 423C (1989).
- [7] R. Kobes, G. Kunstatter, and A. Rebhan, Nucl. Phys. **B355**, 1 (1991).
- [8] E. Braaten and R. D. Pisarski, Nucl. Phys. **B337**, 569 (1990).
- [9] U. Kraemmer and A. Rebhan, Rept. Prog. Phys. **67**, 351 (2004).
- [10] J.-P. Blaizot, E. Iancu, and A. Rebhan, in *Quark-Gluon Plasma 3*, edited by R. C. Hwa and X.-N. Wang (World Scientific, Singapore, 2003).
- [11] J. O. Andersen and M. Strickland, Ann. Phys. **317**, 281 (2005).
- [12] G. D. Moore, JHEP **0210**, 055 (2002).
- [13] A. Ipp, G. D. Moore, and A. Rebhan, JHEP **0301**, 037 (2003).
- [14] A. Ipp and A. Rebhan, JHEP **0306**, 032 (2003).
- [15] J.-P. Blaizot, A. Ipp, A. Rebhan, and U. Reinosa, Asymptotic thermal quark masses and the entropy of QCD in the large- N_f limit, in preparation.
- [16] A. Peshier, K. Schertler, and M. H. Thoma, Annals Phys. **266**, 162 (1998).
- [17] G. Aarts and J. M. Martinez Resco, JHEP **03**, 074 (2005).
- [18] I. T. Drummond, R. R. Horgan, P. V. Landshoff, and A. Rebhan, Nucl. Phys. **B524**, 579 (1998).
- [19] H. J. de Vega and M. Simionato, Phys. Rev. **D64**, 021703 (2001).
- [20] J.-P. Blaizot and E. Iancu, Phys. Rev. **D56**, 7877 (1997).
- [21] E. Braaten and R. D. Pisarski, Phys. Rev. **D45**, 1827 (1992).
- [22] J. Frenkel and J. C. Taylor, Nucl. Phys. **B374**, 156 (1992).
- [23] B. Vanderheyden and G. Baym, J. Stat. Phys. **93**, 843 (1998).
- [24] J.-P. Blaizot, E. Iancu, and A. Rebhan, Phys. Rev. **D63**, 065003 (2001).
- [25] E. Braaten and R. D. Pisarski, Phys. Rev. **D42**, 2156 (1990).
- [26] R. D. Pisarski, Phys. Rev. **D47**, 5589 (1993).
- [27] F. Flechsig, A. K. Rebhan, and H. Schulz, Phys. Rev. **D52**, 2994 (1995).
- [28] P. Romatschke and M. Strickland, Phys. Rev. **D68**, 036004 (2003).
- [29] A. L. Fetter and J. D. Walecka, *Quantum Theory of Many-Particle Systems* (McGraw-Hill, New York, 1971).
- [30] J. Kapusta and T. Toimela, Phys. Rev. **D37**, 3731 (1988).
- [31] A. Ipp, A. Rebhan, and A. Vuorinen, Phys. Rev. **D69**, 077901 (2004).
- [32] J. A. M. Vermaseren, Comput. Phys. Commun. **83**, 45 (1994).
- [33] D. Binosi and L. Theussl, Comput. Phys. Commun. **161**, 76 (2004).
- [34] K. Kajantie and J. Kapusta, Ann. Phys. **160**, 477 (1985).
- [35] U. Heinz, K. Kajantie, and T. Toimela, Ann. Phys. **176**, 218 (1987).
- [36] M. Kitazawa, T. Koide, T. Kunihiro, and Y. Nemoto, Pre-critical phenomena of two-flavor color superconductivity in heated quark matter: Di-quark-pair fluctuations and non-Fermi liquid behavior of quarks, hep-ph/0502035.
- [37] A. Ipp, Quantum corrections to thermodynamic properties in the large N_f limit of the quark gluon plasma, PhD thesis TU Vienna, hep-ph/0405123.